Am J Cancer Res 2022;12(8):3870-3891
www.ajcr.us /ISSN:2156-6976/ajcr0142827

Original Article

Development and validation of a combined ferroptosis- and pyroptosis-related gene signatures for the prediction of clinical outcomes in lung adenocarcinoma

Xuyu Gu[1], Shiyou Wei[2], Bing Chen[3], Wentian Zhang[4], Shiya Zheng[5]

[1]School of Medicine, Southeast University, Nanjing 210009, China; [2]Department of Anesthesiology, Shanghai Pulmonary Hospital, Tongji University School of Medicine, Shanghai 200433, China; [3]Department of Thoracic Surgery, The Affiliated Cancer Hospital of Nanjing Medical University, Nanjing 210009, China; [4]Department of Thoracic Surgery, Shanghai Pulmonary Hospital, Tongji University School of Medicine, Shanghai 200433, China; [5]Department of Oncology, Zhongda Hospital, School of Medicine, Southeast University, Nanjing 210009, China

Received March 12, 2022; Accepted July 28, 2022; Epub August 15, 2022; Published August 30, 2022

Abstract: Lung adenocarcinoma (LUAD) is a very heterogeneous cancer with a bad prognosis. Pyroptosis and ferroptosis are two newly discovered forms of regulated cell death, which can trigger inflammation-related immunosuppression in tumor microenvironments, thereby promoting tumor growth. So far, there has been no thorough systematic investigation of the predictive values of ferroptosis and pyroptosis-related genes in LUAD. Therefore, in this study, we conducted a combined analyses in the gene expression of ferroptosis and pyroptosis and identified four distinct subgroups: immobility, ferroptosis, pyroptosis, and mixed. The gene sets most closely associated to both ferroptosis and pyroptosis were utilized to build a risk prediction model based on their variations in survival and biological activities. More importantly, our conclusions from bioinformatics analyses were validated by external experiments in patients with LUAD. In conclusion, the establishment of LUAD subgroups based on the ferroptosis- and pyroptosis-related gene expression profile provided new insights into understanding the roles of programmed cell death in oncogenesis and might contribute to the development of individualized therapy.

Keywords: Lung adenocarcinoma, ferroptosis, pyroptosis, gene signatures, clinical outcomes

Introduction

Because of its poor prognosis, lung cancer is one of the leading causes of cancer-related mortality globally [1]. Non-small cell lung cancer (NSCLC) accounts for the vast majority of LUAD diagnoses, while the most common NSCLC histologic subtype accounts for around 40% of all lung cancer cases [2]. The two major clinical challenges with LUAD treatment are the late diagnosis and drug resistance [3]. Although multiple clinical trials have demonstrated encouraging effects in certain LUAD patients with immunotherapies based on immune checkpoint inhibitors (ICIs) [4], other LUAD patients who undergo ICI therapy fail to exhibit a significant improvement in OS, probably due to cancer cell resistance to apoptosis. Hence, searching for novel forms of cell death has emerged as a viable treatment strategy.

Apoptosis, necrosis, ferroptosis, parthanatos, oxeiptosis, oncosis, pyroptosis, and autophagy are a few of the several types of cell death that are involved in the pathophysiology and development of cancer. Of note, ferroptosis and pyroptosis have become the center of interest in recent years. Numerous studies have shown that the essential biological processes connected to the development of LUAD are ferroptosis and pyroptosis [7, 8]. In contrast to apoptosis, necrosis, and autophagy, which are other types of programmed cell death [9], ferroptosis is iron-dependent, which is caused by an imbalance in cellular redox equilibrium and ultimately the excessive lipid peroxidation. Many studies

have explored the functional mechanism and the potential of targeting ferroptosis for cancer treatment [10]. For example, Alvarez et al. have reported that decreasing the iron-sulfur cluster biosynthesis enzyme NFS1 in LUAD, in conjunction with limiting cysteine transport, induces ferroptosis in vitro and reduced xenograft tumor growth in vivo [11]. Zhang et al. have discovered that the translational control of SLC7A11 by RBMS1 modifies lung cancer ferroptosis [12]. Wang et al. found that the lung cancer stem cell factor SOX2 mediates ferroptosis resistance by overexpressing SLC7A11 [13]. Other newly identified regulators, such as erianin, may impede cell migration and cause Ca^{2+}/CaM-dependent ferroptosis, potentially playing an anti-tumor role in lung cancer [15].

However, how ferroptosis affects the tumor immune microenvironment (TIME) remains elusive. It is reasonable to speculate the function of ferroptosis in TIME as TIME is connected to iron metabolism and homeostasis in vivo, whereas ferroptosis is necessary for tumor immunity [16]. Recent research has shown that CD8+ T lymphocytes activated by immunotherapy raise ferroptosis-specific lipid peroxidation in tumor cells, increasing the effectiveness of cancer immunotherapy [17]. It's important to note that the expression of SLC7A11 and SLC3A2 is downregulated by IFN secreted by CD8+ T cells, which promotes ferroptosis and lipid peroxidation in addition to blocking tumor cells from absorbing cystine [18]. A connection between ferroptosis and the prognosis of non-small cell lung cancer was also found by Lai et al. [19]. LUAD and their activities are impacted by ferroptosis-related genes, although little is known about the processes behind these effects.

The synthesis of several proinflammatory mediators during pyroptosis, a lytic type of controlled cell death, is one of its defining features [20]. One of two signaling pathways-the GSDMD-dependent, which is regulated by caspase 1/4/5/11, or the GSDME-dependent, which is regulated by caspase 3-can initiate pyroptosis [21-24]. Gasdermin C and Gasdermin D are two important pyroptosis effectors that are overexpressed in several malignancies and are linked to tumor growth and the poor prognosis of patients [25, 26]. Furthermore, Teng et al. discovered that the ROS/NF-κB/NLRP3/GSDMD signal axis was activated by PPVI, the caspase 1-mediated pyroptosis, which mediated the PPVI-induced suppression of NSCLC [27]. Furthermore, by triggering caspase 3/GSDME signaling, Zhang et al. discovered that the chemotherapy medicines paclitaxel and cisplatin differently promote pyroptosis in A549 lung cancer cells [28]. Both in vivo and in vitro, cucurbitacin B reduces NSCLC via causing TLR4/NLRP3/GSDMD-dependent pyroptosis [29]. Significantly, a unique gene signature for pyroptosis was discovered in LUAD to be used in prognostic prediction. The development of LUAD depends on the lncRNA KCNQ1OT1/miR-335-5p/NLRP1/NLRP7-mediated regulatory axis of pyroptosis [30]. Furthermore, Gasdermin E may promote tumor cell phagocytosis by macrophages, enhance the quantity and potency of CD8+ T lymphocytes, and boost the activity of natural killer (NK) cells, leading to tumor cell pyroptosis and generating a positive feedback loop [31].

The interaction among pyroptosis, ferroptosis, and TIME to influence their perspective function is intricate. CD8+ T lymphocytes could limit tumor growth by inducing ferroptosis and pyroptosis via different mechanisms. For instance, CD8+ T cells may release IFN-γ to inhibit SLC7A11 expression, leading to a buildup of lipid ROS and tumor cell ferroptosis [32]. The activation of ferroptosis, in turn, can further improve antitumor immunity. Additionally, in order to cause pyroptosis and activate the macrophage-derived cytokine IL-1, necessary for antitumor immunity, CD8+ T cells may produce GzmA (a GSDMB-cleaving enzyme) and GzmB (a GSDME-cleaving enzyme) [33]. At present, the impact of pyroptosis and ferroptosis on tumor biology is unknown. Therefore, it is critical to better understand the complex functions and the signaling pathways of pyroptosis and ferroptosis in order to develop pyroptosis and ferroptosis-related treatment strategies for LUAD.

In this study, we identified four important cell death subgroups of LUAD based on the consensus clustering of gene expression patterns associated with pyroptosis and ferroptosis. Each of these subgroups was correlated with unique immunological, mutational, and survival markers. The pyroptosis-ferroptosis score was also computed, and it has a greater ca-

pacity to predict the response to chemotherapy and immunotherapy in LUAD patients.

Materials and methods

LUAD datasets and data processing

The Cancer Genome Atlas (TCGA) RNA-sequencing data and comprehensive clinical information for 492 LUAD patients were retrieved via the GDC API. The FPKM (Fragments Per Kilobase per Million) expression data were converted to TPM (Transcripts Per Kilobase per Million) format and utilized as the training cohort. Complete patient clinical information from the GSE30219 dataset based on the Affymetrix HG-U133 Plus 2.0 Array platform, from the GSE72094 dataset based on the Rosetta/Merck Human RSTA Custom Affymetrix 2.0 platform, and from the GSE42127 dataset based on the Illumina HumanWG-6 v3.0 expression beadchip platform were downloaded from GEO (http://www.ncbi.nlm.nih.gov/geo/) database and used as the test cohorts. In addition, two immunotherapy cohorts, GSE126044 and GSE135222, consisting of patients who underwent PD1 treatment were used for the prediction of immunotherapeutic responses. The IMvigor210 dataset was publiclyavailable, and the fully described software and packages downloaded at http://research-pub.gene.com/IMvigor210CoreBiologies were distributed under the Creative Commons 3.0 license. A total of 298 melanoma patients who received PD1 therapy and had full clinical data related to their diagnoses were included.

Somatic cell data collection

The TCGA-LUAD cohort's somatic mutation data (in MAF format) were obtained from the UCSC Xena Data Center (https://xena.ucsc.edu). The maftools package in R was used to evaluate and illustrate the mutation type and frequency of the genes. In addition, copy number variants (CNV) in TCGA-LUAD patients were collected and analyzed; a score > 0.2 was defined as amplification, while the score < -0.2 was defined as deletion. The CNV summary map was visualized using the Circos package in R.

Pyroptosis and ferroptosis subgroups

The pyroptosis-related genes (n = 39) [34-36] and the ferroptosis-associated genes (n = 113) [37-39] were collated from published literatures as shown in Table S1. The ConsensusClusterPlus package was used to cluster the pyroptosis- and ferroptosis-related genes (set parameters were as follows: reps = 1000, pItem = 0.8, and pfeature = 1). Ward. D 2 and Pearson correlation were used as the clustering algorithm and distance measure, respectively, with k = 5. The median expression levels of co-expressed pyroptosis and ferroptosis genes were used to divide samples into the subgroups shown below: immobility, pyroptosis, ferroptosis, and mixed.

Development and verification of risk model based on subgroups

The risk model was built using samples from the TCGA database. The WGCNA tool in R was used to create a scale-free co-expression network, and the transcriptome was utilized to identify the most significant modules for the cell death subgroups. To increase matrix similarity, a soft threshold parameter of 12 (scale-free $R^2 = 0.91$) was used, and a scale-free co-expression network was built. Hierarchical clustering of the weighted coefficient matrix was used to identify the modules further. The genes in the pink module most associated with subgroups were used for further analyses. Univariate analysis and the log-rank test were used to find the pertinent prognostic modular genes. The Cox proportional hazard model (iteration = 100) with LASSO penalty function was utilized for these possible prognostic genes, and the optimal gene model was chosen using R's glmnet package. The best gene model was used to determine risk ratings using the following formula:

$$\text{Risk Score} = \sum i \; Coefficient(mRNA_i) \times Expression(mRNA_i)$$

Moreover, the consistency C-index, proposed by Harrell et al. was calculated using the survcomp package in R [37-39], and the predictive powers of all the five datasets for scoring were validated; the higher the C-index, the more accurate the model's prediction capacity.

Predicting chemotherapeutic and immunotherapeutic responses

The pRRophetic package in R and the Genomics of Drug Sensitivity in Cancer (GDSC) data-

base were used to choose the five first-line therapeutic medicines utilized in the treatment of LUAD: cisplatin, gemcitabine, paclitaxel, docetaxel, and vinorelbine. The half-maximal inhibitory concentration (IC50) for each sample and the sensitivity of the high- and low-risk groups to chemotherapy were compared using ridge regression (RR). The Tumor Immune Dysfunction and Exclusion (TIDE) algorithm and subclass mapping were used to forecast how patients in different risk categories will respond to anti-CTLA4 and anti-PD1 treatment. In addition, the potentil treatment targets included genes that substantially varied between the high- and low-risk groups. The CMap database (https://clue.io/) was used to look for prospective medications that may target these genes. As a result, in addition to choosing the anticipated drugs based on gene expression characteristics, the mode of action (MOA) of these pharmaceuticals targeting the relevant biochemical pathways was also determined. The compounds with concentration fraction < -96 were considered potential therapeutic drugs.

qRT-PCR

To verify the prediction accuracy, qRT-PCR was used to examine the expression levels of the critical genes such as ANLN, E2F7, ECT2, HMMR, and TK1 in thirty-six LUAD clinical samples and their paired adjacent normal lung tissues obtained from the Shanghai Pulmonary Hospital. The total RNA was extracted using the Trizol reagent, and its quality was confirmed by RNA gel electrophoresis. Then, 2 μg of the total RNA was transcribed into cDNA using a quantitative reverse transcription kit (Wuhan Seville biology company) followed by qPCR analysis. The preparation of qPCR reaction was according to the manufacturer's instructions. Briefly, the fluorescence quantitative PCR kit SYBR Green qPCR Master Mix (Wuhan Seville biology company) was used, and the PCR reaction conditions were as follows: pre-denaturation at 95°C for 10 min; denaturation at 95°C for 10 seconds; annealing at 60°C for the 40 seconds, and final extension at 72°C for 40 seconds. Forty cycles were set for the qPCR reaction. The CT values were recorded, and the relative expressions were calculated using the quantitative $2^{-\Delta\Delta CT}$ method with GADPH as internal reference. The sequences of primers used in this study were listed in Table S2. This study was approved by Shanghai Pulmonary Hospital Ethics Committee (ethical lot number: K21-111Y).

Immunofluorescence staining

Formalin fixed, paraffin-embedded tissue blocks of LUAD and the corresponding paracancerous tissues were cut into 5-μm-thick sections. These sections were dewaxed, rehydrated, and incubated with primary antibodies against ANLN, EEF7, ECT2, HMMR, and TK1, followed by incubation with FITC-conjugated secondary antibodies. And DAPI (sigma) was used for nuclear counterstaining. The sections were examined under fluorescence microscope (Zeiss, Oberkochen, Germany) and photographed. The intensity of fluorescence staining of the sections was determined by Image J.

Bioinformatics and statistical analyses

The CIBERSORT package in R and LM22 characteristics were used to calculate the infiltration levels of 22 immune cell types in each patient in the TCGA cohort. The immunological and matrix scores for each sample were calculated using the ESTIMATE program. The GSVA program in R was used to assess the activity of immune-related pathways in each sample using the ssGSEA method. Gene markers for immune-related pathways are provided in Table S3. Next, the differentially expressed genes were obtained using the Limma package, and those with P.adjust < 0.05 and |Log2FC| > 1 were considered as significantly differentially expressed. The clusterprofiler software in R and the Metascape webtool (https://metascape.org/gp/index.html) were used to annotate gene functions. R program was used for all statistical analysis and mapping (version 4.04). For the above-mentioned two groups, the Kruskal-Wallis test was performed, and the Wilcoxon test was utilized for pairwise comparison. The Chi-Square test was used to compare proportional differences. To assess the survival curves for subgroups in each dataset, Kaplan-Meier curves were produced. To determine statistically significant differences, the logarithmic rank test was applied. The survivalROC package in R was used to conduct the time-dependent receiver operating characteristic (tROC) analysis, and the area under the curve (AUC) was determined to assess the predictive potential of variables. The rms package in R was used to plot nomograms and calibration curves.

The Student's t-test was performed to examine gene expression changes between tumor and normal tissues. Unless specified, two-tailed $P < 0.05$ was considered statistically significant for all tests.

Results

Identification of four distinct subgroups by combined analysis of ferroptosis and pyroptosis gene expression in LUAD

In total, 492 patients from the TCGA-LUAD cohort were included in our study. The LUAD tumors were classified based on the relative expression levels of ferroptosis- and pyroptosis-related genes. To select the co-regulated and biologically relevant genes in LUAD, we performed consensus clustering and identified two sets of stably co-expressed genes involved in the pyroptosis (N = 20) and ferroptosis (N = 66) pathways for cell death subgrouping as shown in **Figures 1A**, S1A-C. For each sample, the median values of pyroptosis and ferroptosis gene co-expression were computed and used to stratify four distinct subgroups: immobility (Pyroptosis ≤ 0, Ferroptosis ≤ 0), pyroptosis (Pyroptosis > 0, Ferroptosis ≤ 0), ferroptosis (Pyroptosis ≤ 0, Ferroptosis > 0), and mixed (Pyroptosis > 0, Ferroptosis > 0) (**Figure 1B**). **Figure 1C** showed the expression levels of pyroptosis and ferroptosis genes in each subgroup. Pyroptosis subgroup was the largest subgroup (148/492; 30.08%), followed by the ferroptosis (132/492; 26.83%), immobility (122/492; 24.80%), and mixed subgroup (90/492; 18.29%). As shown in **Figure 1D**, based on the survival analysis, the pyroptosis subgroup was associated with the best overall survival, while the ferroptosis and mixed subgroups exhibited the worst overall survival. The intersection of differentially expressed genes among these four subgroups was shown in Figure S1D and Table S4.

Association between these four subgroups and the immunophenotype

As shown in **Figure 2A**, the ferroptosis subgroup showed the highest tumor homogeneity and the lowest immune score as indicated by the ESTIMATE scores, while the pyroptosis subgroup was the opposite, exhibiting the lowest homogeneity and the highest immune score. We also examined the differential expression of immune checkpoint related genes, including CD274, HAVCR2, CTLA4, LAG3, IDO1, and PDCD1, and the immune response related genes, including CD8A, CXCL9, CXCL10, GZMA, GZMB, PRF1, IFNG, TNF, and TBX2 among the subgroups [41, 42]. As shown in **Figure 2B**, their expressions were higher in the pyroptosis and mixed subgroups, while their expressions were the lowest in the ferroptosis subgroup. Next, the abundance of 22 immune cell types was quantified using a cyclic classification algorithm. **Figure 2C** showed the differences in levels of immune cell infiltration among the subgroups. CD8+ T cells and memory B cells showed higher infiltration in the pyroptosis subgroup. A greater infiltration of naive B cells and activated dendritic cells in the ferroptosis subgroup was observed.

Furthermore, we analyzed the differences in immunoreactive pathways among the subgroups (**Figure 2D**). Immunoreactive pathways were more active in the pyroptosis and mixed subgroups, while was the lowest in the ferroptosis subgroup, suggesting the significant differences in immunoactivities among the subgroups, which might attribute to the survival of patients. Moreover, through the enrichment analysis of the differentially expressed genes among subgroups, we found a significant enrichment in immune-related pathways, including the immunoregulatory interactions between a lymphoid and a non-lymphoid cell, immune system processes, and positive regulation of immune responses (**Figure 2E**). The interaction network among the enrichment pathways was shown in **Figure 2F**, among them, pathways related to lymphocyte activation, immune effector process, regulation of cytokine production, and leukocyte migration were highly enriched. Based on these data, we postulated that pyroptosis, a highly immunogenic type of cell death, might trigger local inflammation and attracted inflammatory cells into the area, which might serve as a potential therapeutic target to reverse TIME's immunosuppression and trigger a systemic immune response to LUAD. In contrast, the ferroptosis subgroup showed the highest tumor homogeneity and the lowest immune score, which might attribute to its poor prognosis.

Association of the cell death subgroups with genomic changes

It has been well known that genetic alterations influence tumor immunity and immune inva-

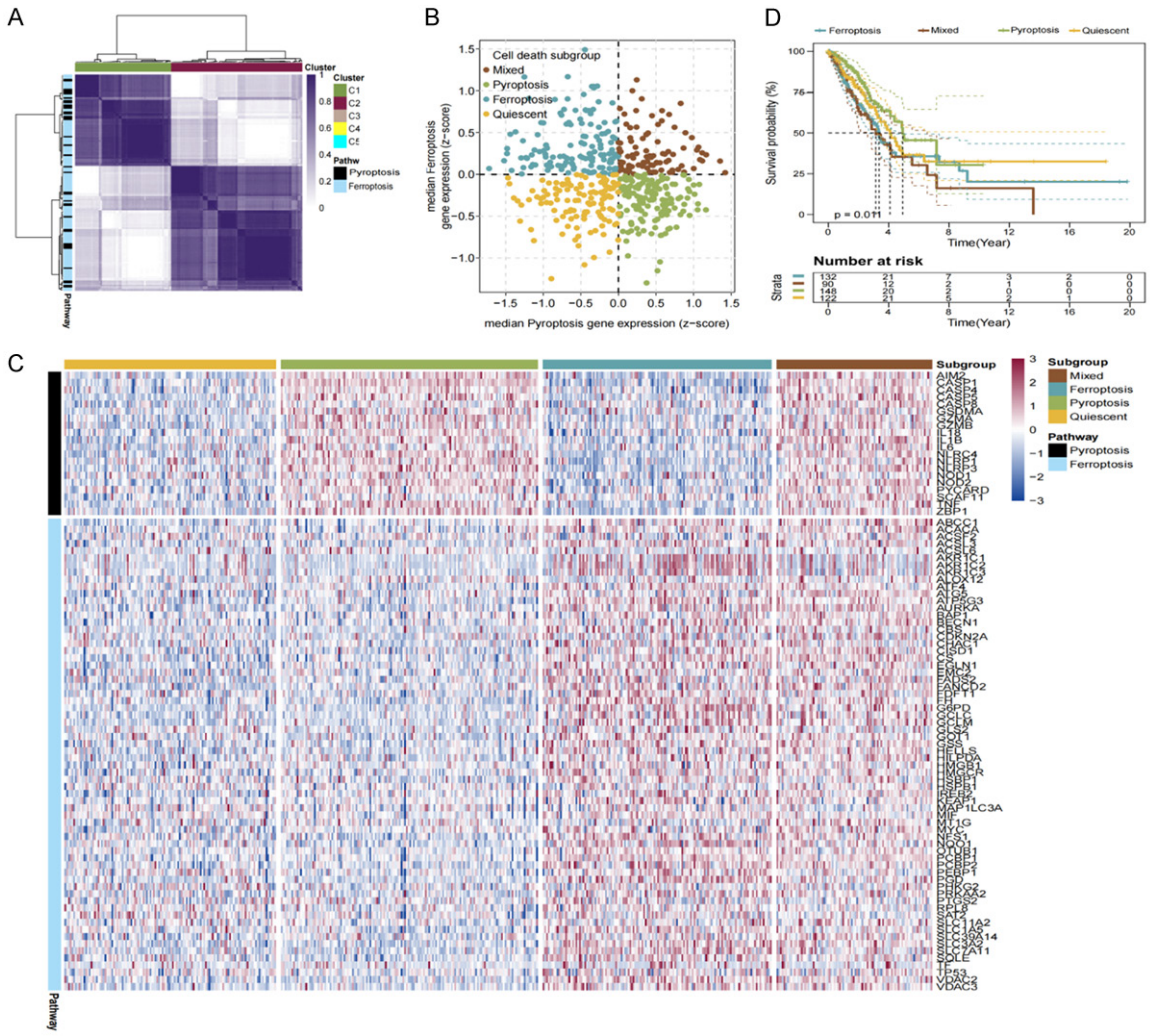

Figure 1. Tumor stratification for LUAD based on relative expression levels of pyroptosis- and ferroptosis-related genes. A. The heat map depicted a consistent clustering solution generated for pyroptosis- and ferroptosis-related genes (k = 2) in 492 patients with LUAD. B. The scatter map showed the median expression levels of pyroptosis- (x-axis) and ferroptosis-related (y-axis) gene co-expression in each LUAD sample. The metabolic subgroups were allocated according to the relative expression levels of pyroptosis- and ferroptosis-associated genes. C. The heat map depicted the co-expression levels of pyroptosis- and ferroptosis-associated genes in each subgroup. D. Kaplan-Meier survival analysis for four subgroups of LUAD patients.

sion. Therefore, we analyzed the differences in copy number variations and somatic variations among the subgroups and found a higher tumor mutation burden (TMB) in ferroptosis and mixed subgroups, while a lower TMB in the pyroptosis and immobility subgroups (**Figure 3A**). In addition, the ferroptosis subgroup had the highest numbers of chromosomal amplifications and deletion events, while the pyroptosis subgroup had the least incidence (**Figure 3B**, **3C**). The mutation landscape of the top 25 most commonly mutated genes in distinct subgroups was shown in **Figure 3D**. Furthermore, we evaluated the correlation between the expression of TP53 and TTN, the top two highest mutated genes, and the median expression of pyroptosis- and ferroptosis-related genes. As shown in **Figure 3E-H**, a positive correlation between TP53 and ferroptosis genes, a negative correlation between TTN and ferroptosis genes, and no significant correlations between either TP53 or TTN with pyroptosis genes were observed. These results suggested that the ferroptosis subgroup showed greater genomic alterations than the pyroptosis subgroup. Taken together, the tight association between fer-

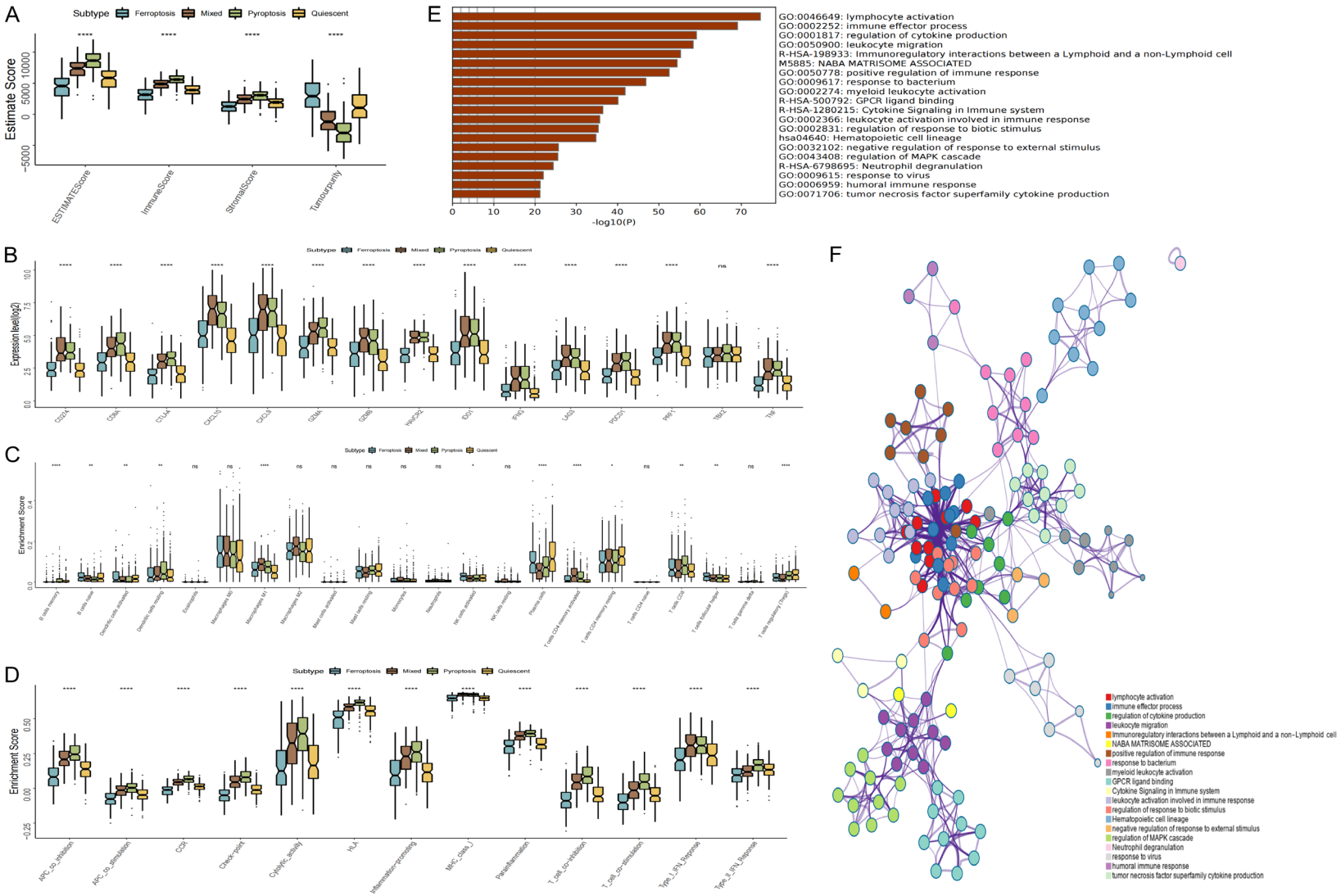

Figure 2. Systematic immune and functional enrichment analyses for the immune subgroups. (A-D) Box diagram of analyses for ESTIMATE score (A), immune checkpoint (B), immune infiltration (C), immune pathways (D) among the subgroups. *P < 0.05; **P < 0.01; ***P < 0.001; ****P < 0.0001. (E) GO functional enrichment analysis, including significantly enriched biological processes, cellular components, molecular functions, and KEGG pathways. (F) Interaction network between the enrichment pathways.

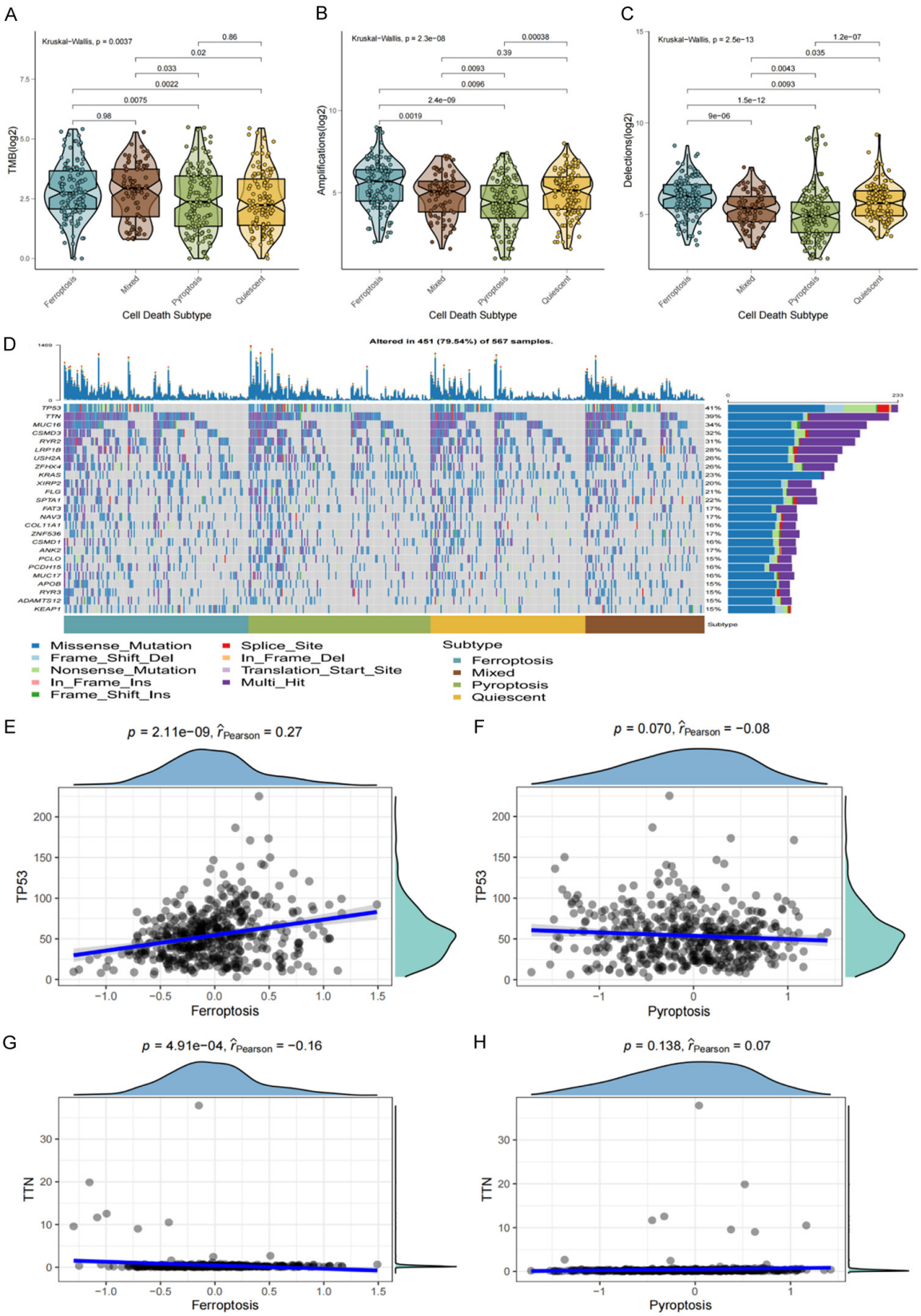

Figure 3. Tumor immune microenvironment patterns and immunogenic characteristics of LUAD associated with the cell death subgroups. A-C. Violin plots for death subgroups in individual LUAD sample were sectioned according to TMB, amplitudes, and deletions. D. Mutation landscape of the top 25 genes with the highest mutation frequency

in different subgroups. E, F. Scatterplot plots delineated the association of the median TP53 gene expression with ferroptosis (left panel) and with pyroptosis (right panel). G, H. Scatterplot plots delineated the associations of the median TTN gene expression with ferroptosis (left panel) and with pyroptosis (right panel).

roptosis and mutations may result in high tumor malignancy, thereby leading to worse prognosis of patients in ferroptosis subgroup.

Construction of risk model based on the subgroups

Given the significant differences in survival and biological functions among the subgroups, we further analyzed the differentially expressed genes. WGCNA was performed in the training cohort using the transcriptomic data for the differentially expressed genes and the subgroups. Using β = 12 as the best soft threshold, we ensured non-scale co-expression in the network graph (Figure S2A), and a total of eight non-gray module graphs were obtained (Figure S2B, S2C). Among these modules, the pink module (R = 0.43, P = 3e-21), with the highest correlation, was considered the most relevant for the cell death subgroups (Figure S2D, S2E). Furthermore, for the 189 genes in the pink module, univariate Cox analysis and the log-rank test were done, and 142 of them were shown to have substantial prognostic predicting capacity (P < 0.05). The detailed data was presented in Table S5. Furthermore, we performed a total of 100 iterations and included two gene sets for further analysis (Table S6). We identified a robust five gene signature: ANLN, E2F7, ECT2, HM, and TK1, as the frequency of the model was significantly higher (**Figure 4A**). As a result, the five-gene signature was best suited for the risk model's creation. Accordingly, the risk score graphs (Figure S2F, S2G) were plotted, and the specific coefficient values were shown in Table S7. To evaluate the effectiveness of our risk score, we first calculated the C-index for predicting the OS, and the values for TCGA, GSE30219, GSE42127, and GSE72049 were 0.6383, 0.6580, 0.6302, and 0.5989, respectively. The tROC analysis showed that the AUC of the risk score plots for each point in the four cohorts for five years was greater than 0.6 (**Figure 4B**). Thus, the risk model had a high prediction accuracy for survival. According to KM analysis, the prognosis of patients in the high-risk category was poorer (P < 0.0001) (**Figure 4C**), and a poor survival was observed in the high-risk group (**Figure 4D**). ROC analysis showed that 1-, and 8-year AUC was 0.71 and 0.68, respectively, suggesting the better prognostic efficacy of risk score (**Figure 4E**). Consistently, similar results were observed in the three test cohorts (Figure S3). **Figure 4F** showed the expression of genes in different subgroups according to the model.

Validation of the independent prognostic value of the risk model

According to the Chi-Square test, all variables except sex revealed significant differences between the high and low subgroups among the differences in each clinical characteristic across subgroups, as shown in **Figure 5A**. Risk score had higher prognostic accuracy than sex, age, and stage (**Figure 5B**). Following the incorporation of new clinical data, univariate and multivariate Cox regression analysis for the four cohorts revealed that the risk score was an independent prognostic predictor (**Figure 5C**, **5D**). In addition, the subgroup analysis showed that the risk score of different clinical subgroups exhibited satisfactory predictive efficacy in four cohorts (Figure S4). Therefore, we constructed a nomogram to better visualize the predictive power of the model (**Figure 5E**), and the calibration curve, the indication of the good predictive accuracy of the nomogram, was presented in **Figure 5F**. Importantly, ROC analysis showed that the nomogram model had the best prediction accuracy as compared to other variables (**Figure 5G**).

Differences in biological functions among the subgroups

We also evaluated the association between our risk score and numerous biological processes. As shown in **Figure 6A**, a high negative correlation was obsesrved between the mean risk score and the immune score (Pearson Correlation = -0.166, P < 0.01). The high-risk group exhibited higher tumor homogeneity and lower immune activity (**Figure 6B**), and most of the immune checkpoint and immunoreactivity characteristics were highly enriched in the high-risk group, in addition to TBX2 (**Figure 6C**). In supporting this, LUAD patients in the two

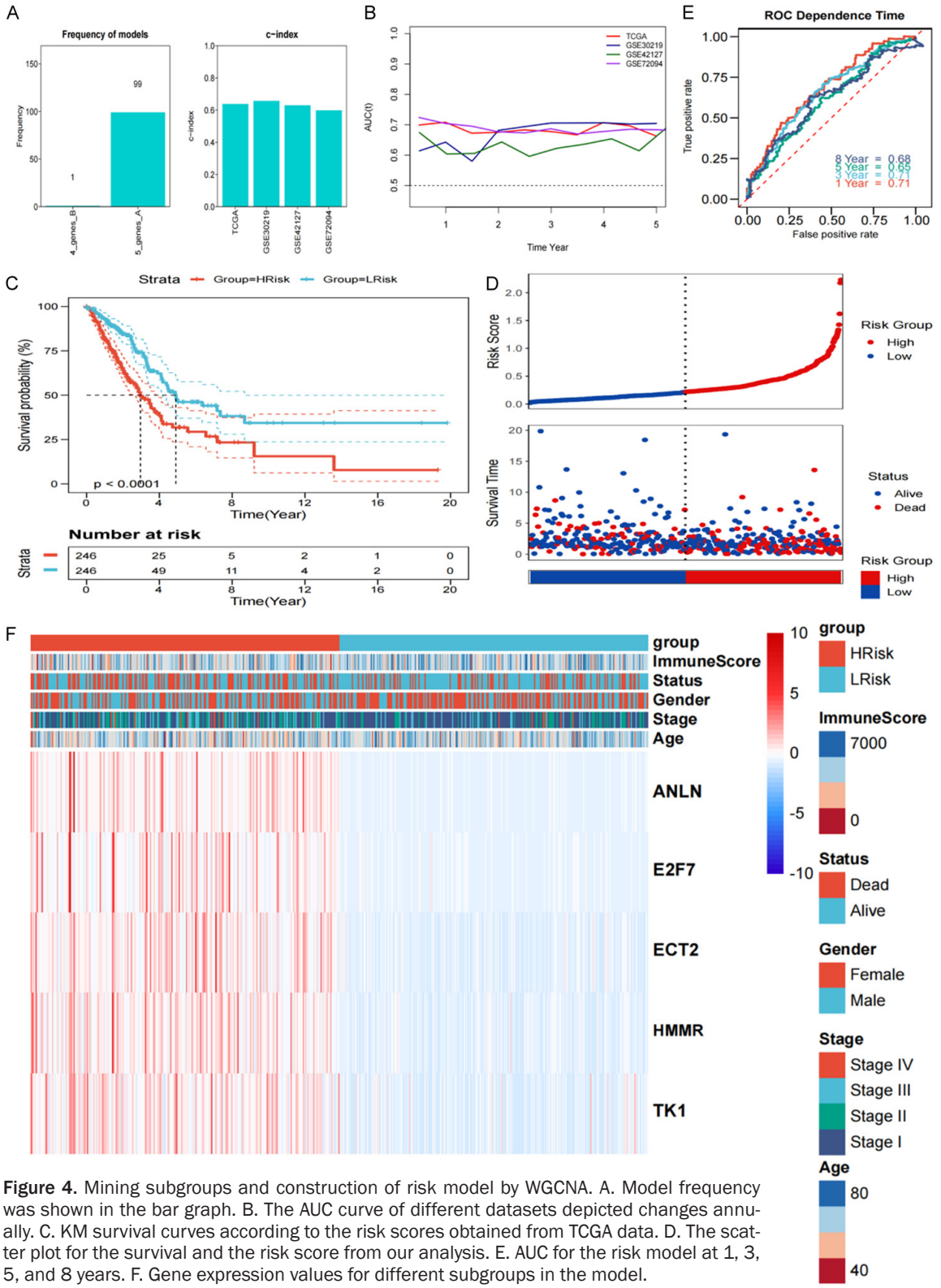

Figure 4. Mining subgroups and construction of risk model by WGCNA. A. Model frequency was shown in the bar graph. B. The AUC curve of different datasets depicted changes annually. C. KM survival curves according to the risk scores obtained from TCGA data. D. The scatter plot for the survival and the risk score from our analysis. E. AUC for the risk model at 1, 3, 5, and 8 years. F. Gene expression values for different subgroups in the model.

groups showed differences in immune microenvironment (**Figure 6D**). The high-risk group showed higher M0/M1 macrophage activated-CD4 cells infiltration, while the low-risk group had higher infiltration of B cells, dendritic cells, mast cells, plasma cells, CD4 resting cells, and

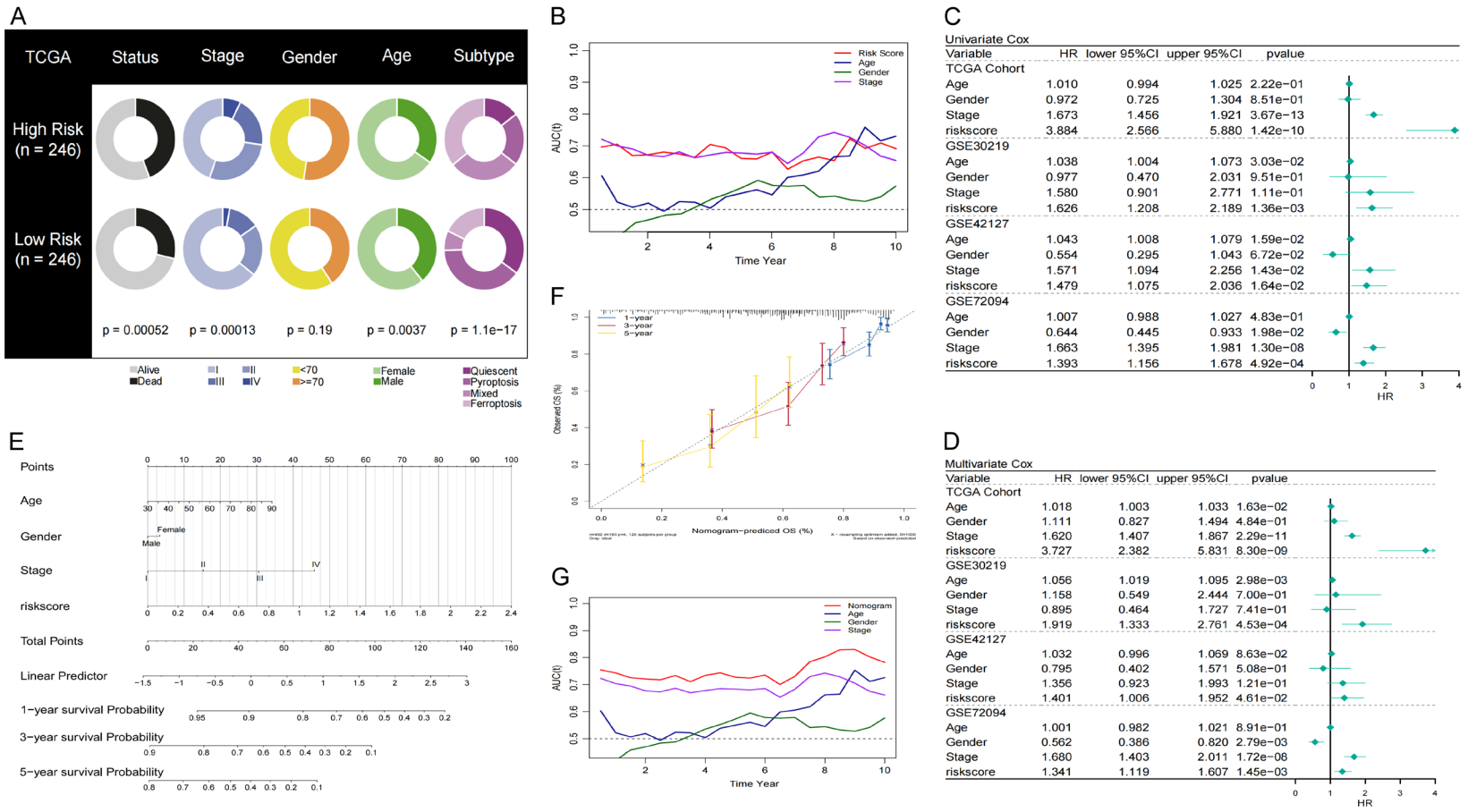

Figure 5. Effectiveness of the risk model. A. Pie chart showing the differences for each clinical variable among subgroups. B. The time-dependent AUC showed the prediction efficiency of risk score and clinical features (Risk score, Age, Gender, and Stage) for OS in training cohort. C, D. Univariate and multivariate forest plots constructed based on the risk model scores and other clinical variables from TCGA data. E. Nomograms based on risk model scores and other clinical variables. F. Rectification curves for nomograms. G. Prediction accuracy of AUC curves of the nomograms.

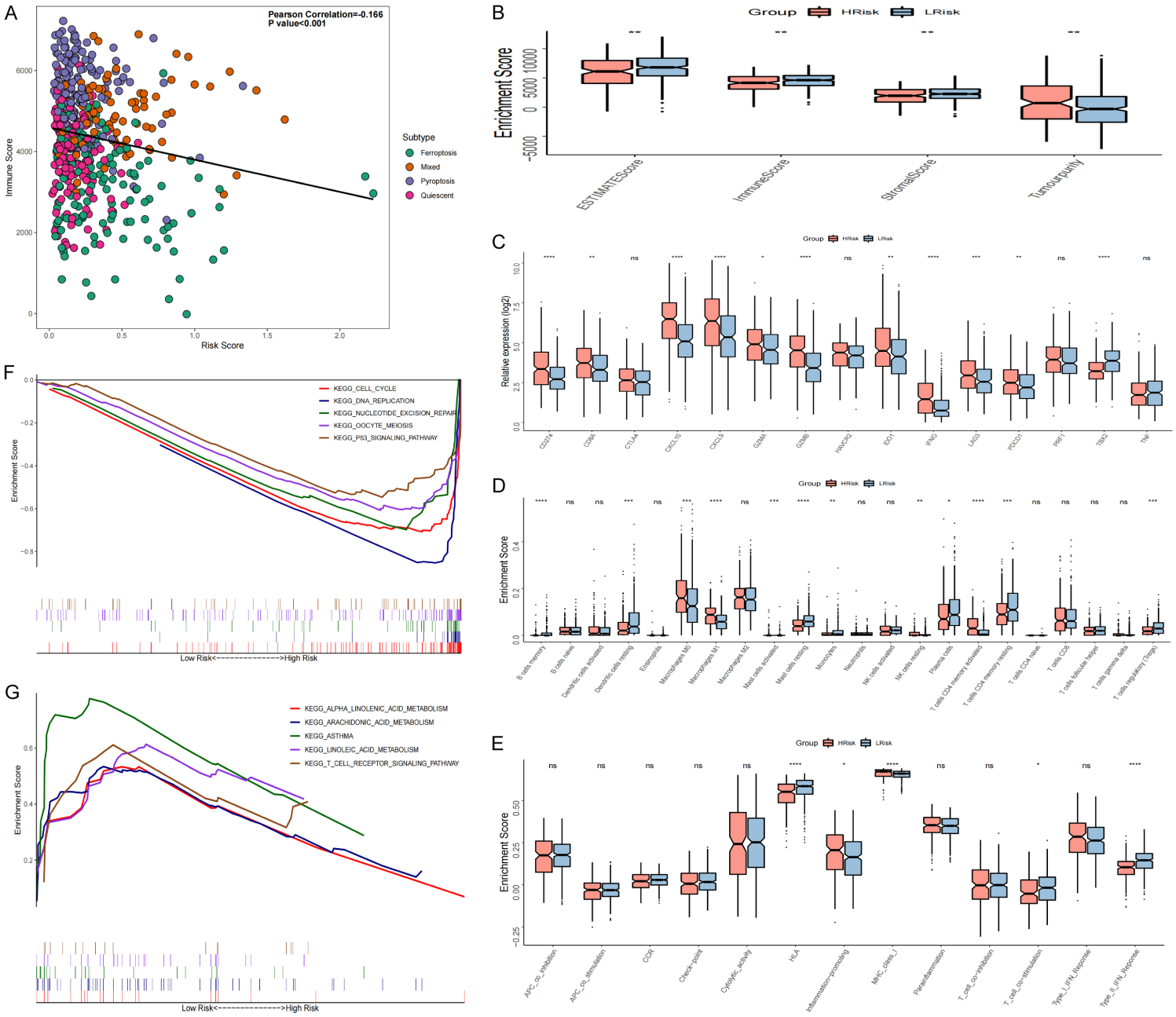
A
Pearson Correlation=-0.166
P value<0.001
Immune Score
Risk Score
Subtype
Ferroptosis
Mixed
Pyroptosis
Quiescent
B
Group HRisk LRisk
Enrichment Score
ESTIMATEScore
ImmuneScore
StromalScore
Tumour purity
C
Relative expression (log2)
CD274
CD8A
CTLA4
CXCL10
CXCL9
GZMA
GZMB
HAVCR2
IDO1
IFNG
LAG3
PDCD1
PRF1
TBX2
TNF
D
Enrichment Score
B cells memory
B cells naive
Dendritic cells activated
Dendritic cells resting
Eosinophils
Macrophages M0
Macrophages M1
Macrophages M2
Mast cells activated
Mast cells resting
Monocytes
Neutrophils
NK cells activated
NK cells resting
Plasma cells
T cells CD4 memory activated
T cells CD4 memory resting
T cells CD4 naive
T cells CD8
T cells follicular helper
T cells gamma delta
T cells regulatory (Tregs)
E
Enrichment Score
APC_co_inhibition
APC_co_stimulation
CCR
Check-point
Cytolytic_activity
HLA
Inflammation-promoting
MHC_class_I
Parainflammation
T_cell_co-inhibition
T_cell_co-stimulation
Type_I_IFN_Reponse
Type_II_IFN_Reponse
F
Enrichment Score
KEGG_CELL_CYCLE
KEGG_DNA_REPLICATION
KEGG_NUCLEOTIDE_EXCISION_REPAIR
KEGG_OOCYTE_MEIOSIS
KEGG_P53_SIGNALING_PATHWAY
Low Risk<----------->High Risk
G
Enrichment Score
KEGG_ALPHA_LINOLENIC_ACID_METABOLISM
KEGG_ARACHIDONIC_ACID_METABOLISM
KEGG_ASTHMA
KEGG_LINOLEIC_ACID_METABOLISM
KEGG_T_CELL_RECEPTOR_SIGNALING_PATHWAY
Low Risk<----------->High Risk

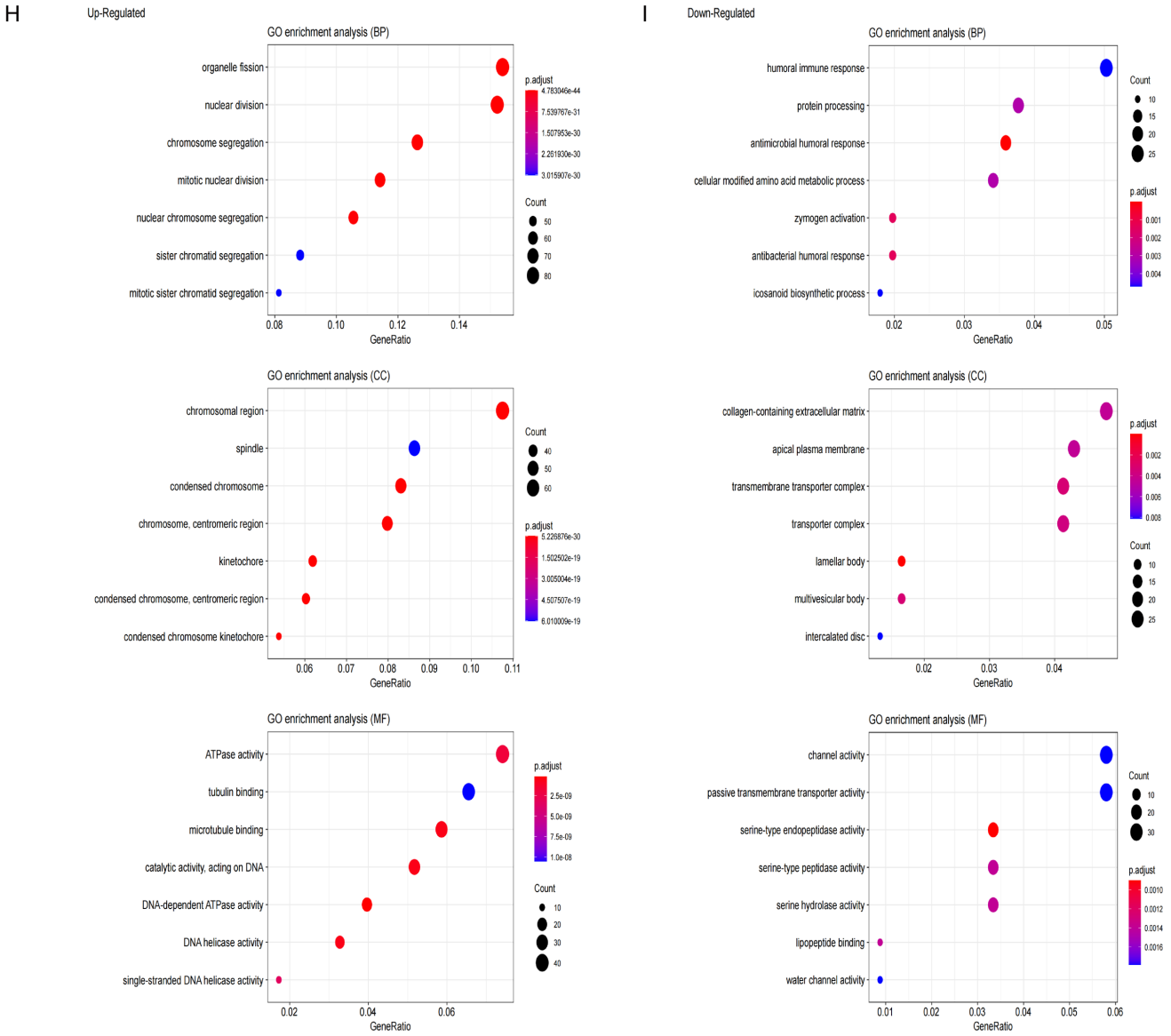

Figure 6. Immunological and functional enrichment analyses for different risk groups. (A) Scatter plot of correlation between immune score and risk score; (B-E) Differences between high and low-risk groups in ESTIMATE score (B), immune checkpoint (C), immune infiltration (D), immune pathways (E). *p < 0.05; **p < 0.01; ***p < 0.001; ****p < 0.0001; (F, G) GSEA analysis for up- and down-regulated genes in high- and low-risk groups; (H, I) GO pathway analysis for up- and down-regulated genes in high and low-risk groups.

Tregs, suggesting active antigen presentation in the low-risk group. Although M0 and M1 macrophages are generally considered to produce antineoplastic proinflammatory cytokines, including ROS and nitric oxide (NO), to inhibit tumor growth and progression [41, 42], M0/M1 macrophage infiltrations may also lead to a poor prognosis. For instance, a recent study showed that M1 macrophage recruitment was strongly associated with poor OS in medulloblastoma [44]. In our study, we further analyzed the balance between M1 and M2 macrophages in the high- and low-risk group, however, the difference was not statistically significant. A possible explanation for higher M0 and M1 macrophage infiltrations in the high-risk group is that pyroptosis and ferroptosis-related genes can regulate the tumor immune microenvironment. To test this, we analyzed the differences in immune response pathways between high- and low-risk groups and found that the MHC class I pathway was significantly upregulated in the high-risk group, while the HLA pathway and type II IFN response pathway were significantly enriched in the low-risk groups (**Figure 6E**). Furthermore, GSEA analysis revealed that cell cycle, DNA repair, and P53 signaling pathways were significantly enriched in the high-risk group, indicating active cell division and tumor malignancy, whereas asthma and T cell receptor pathways were enriched in the low-risk group, indicating the immune system's active state (**Figure 6F**, **6G**). Further enrichment analysis revealed that the up-regulated genes in high-risk groups were strongly related with cell division processes such as organelle fission, nuclear division, and chromosomal segregation. The down-regulated genes were associated with immune activity and protein production processes, including humoral immune response, antimicrobial humoral response, and protein processing (**Figure 6H**, **6I**).

Differences in genomic alterations among the subgroups

We examined at whether there were any differences in total mutation counts, nonsynonymous mutation counts, and synonymous mutation counts between the high- and low-risk groups (**Figure 7A-C**). There was a positive correlation between the risk score and the mutation load among the three mutation types; when the mutation load was higher, its correlation with all mutation counts was the lowest (R = 0.23, P = 2e-07), whereas its correlation with the synonymous mutation counts was the highest (R = 0.29, P = 0.89e-11) in the high-score group. The general topography of copy number differences in the high- and low-score groups was shown in **Figure 7D** and **7E**. **Figure 7F** and **7G** revealed that the high-score group had a considerable increase in amplifications and deletions. We also examined the mutations in the top 25 most mutated genes between the high- and low-score groups. As shown in **Figure 7H**, all the genes with significant differences had higher mutation rates in the high-score group. **Figure 7I** showed the landscape of mutations for the top 25 genes between high- and low-score groups.

Risk score as an indicator to guide treatment strategies

The sensitivity to five regularly used chemotherapy medications was compared between high- and low-score groups, and we discovered that the IC50 of these drugs was considerably greater in the low-score group, indicating a reduced sensitivity to chemotherapy (**Figure 8A**). The three external validation cohorts yielded similar findings. Because the differentially expressed genes between high- and low-score groups might be used as small chemical targets, we performed MOA analysis to identify 66 small molecule drugs targeting 39 molecular pathways (Figure S5A). **Figure 8B** showed a significant reduction in risk scores for patients who were responding to immunotherapy in the external dataset GSE126044 upon PD1 treatment. The survival analysis indicated that the overall survival was the worst in the NSCLC dataset of GSE135222 upon PD1 treatment in the high-score group (P = 0.0061) (**Figure 8C**). The risk score's usefulness was further evaluated in the IMvigor210 cohort, which revealed that responders had lower scores (**Figure 8D**). **Figure 8E** demonstrated that patients with high scores had the worst overall survival. Consistently, the Chi-Square test also showed that the response rate to PD1 was higher in the low-score group (P = 0.013) (**Figure 8F**), and patients in the low-score group were sensitive to the PD1 treatment (FDR = 0.014) according to the subclass mapping algorithm (**Figure 8G**). TIDE algorithm also similarly showed that the low score group was more sensitive to PD1

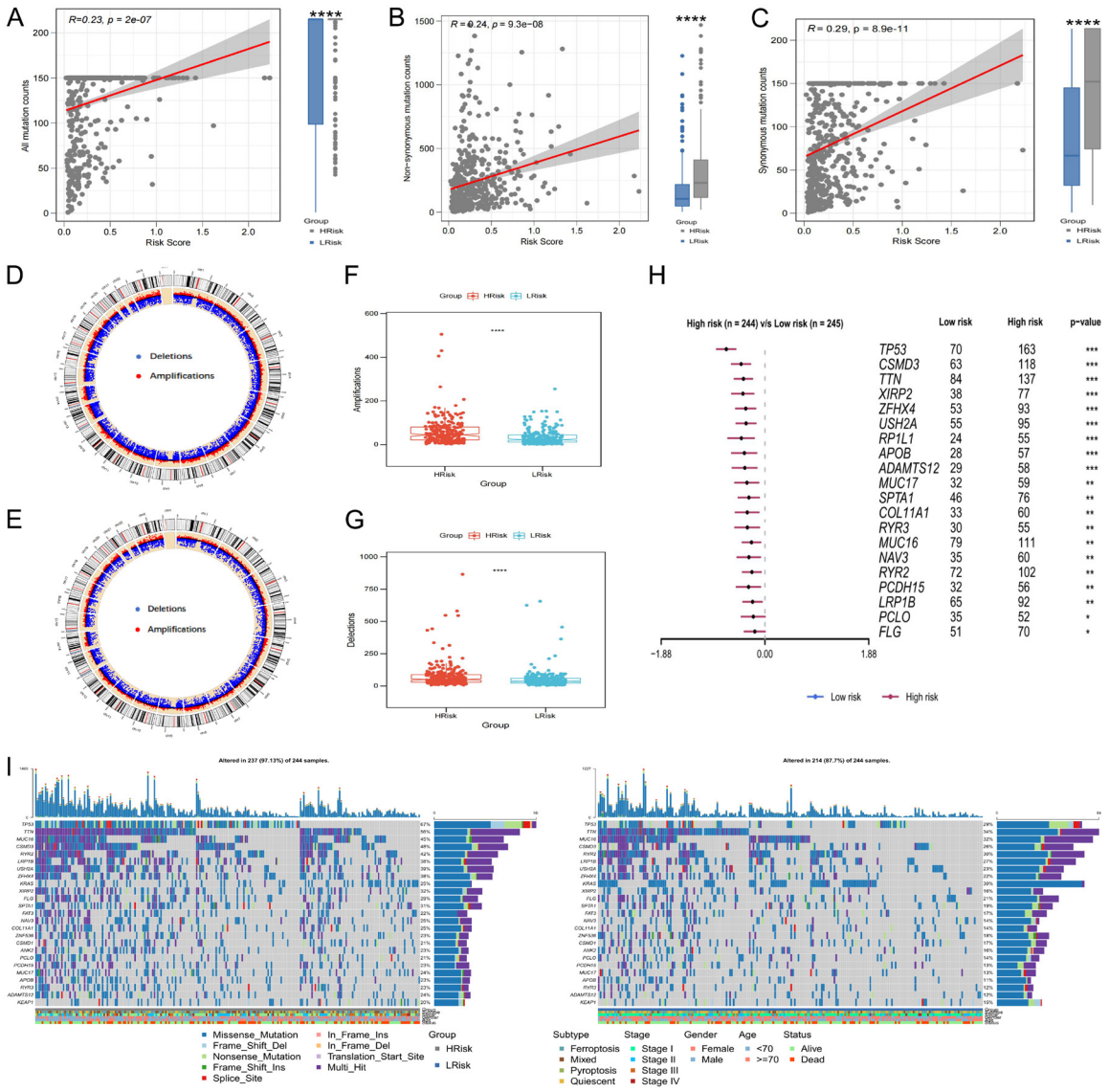

Figure 7. Differences in genomic mutations among different subgroups and the mutational landscape. A-C. Scatter plots based on the differences on all mutation counts, non-synonymous mutation counts, and synonymous mutation counts between the high- and low-risk groups. *p < 0.05; **p < 0.01; ***p < 0.001; ****p < 0.0001; D, E. Overall landscape for copy number variations in the high- and low-risk score groups; F, G. Amplification and deletion variations were significantly greater in the high-risk score group; H. Mutation difference forest plot of the 25 genes with the highest mutation frequency in the high- and low-risk groups. All significantly different genes had higher mutation frequencies in the high-risk group (*P < 0.05; **P < 0.01; ***P < 0.001); I. Oncoplot of mutation landscape for the top 25 frequently mutated genes between high- and low-risk score groups.

treatment (P = 0.015) (**Figure 8H**). Consistent results were observed in the three validation cohorts (Figure S5B-D).

Validation of five hub genes in the clinical samples

To validate the accuracy and reliability of this signature, tumor samples and the paracancerous tissues from 36 newly diagnosed LUAD patients were collected and analyzed by qRT-PCR, and the differential expression of the five hub genes was compared by utilizing the paired t-test. The results showed that the expressions of ANLN, E2F7, ECT2, HMMR, and TK1 in LUAD were significantly up-regulated in tumor samples compared to those in paracancerous tissues (**Figure 9A-E**), which supported our conclusions from bioinformatics analyses. We

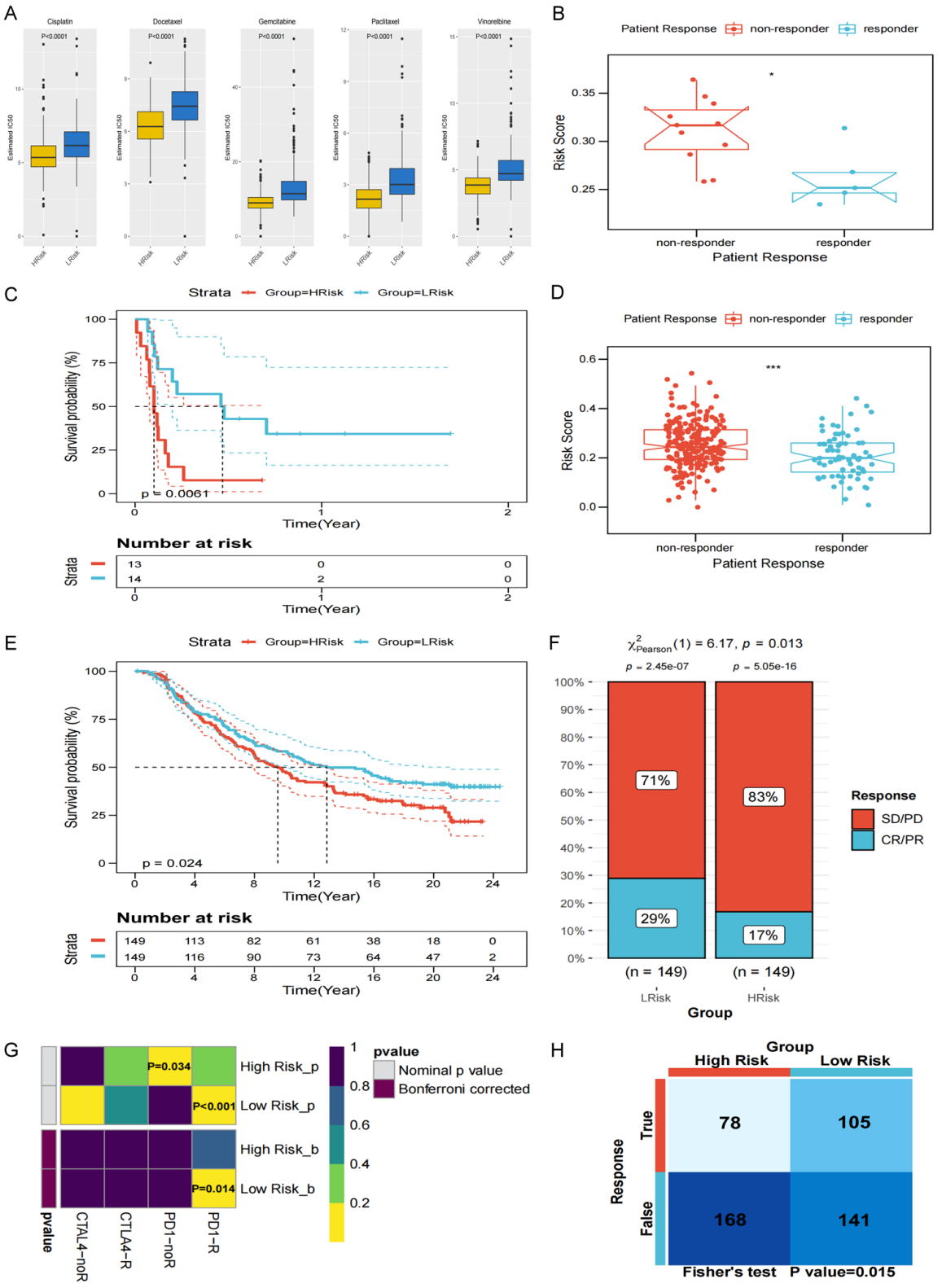

Figure 8. Correlation between risk score and drug sensitivity. A. Differences in the IC50 values of five commonly used drugs between the high- and low-score groups; B. Differences in risk scores between responders and non-responders; C. The KM survival curve for the high- and low-score groups of patients in the GSE135222 data; D. Differences in risk scores between responders and non-responders in the IMvigor210 dataset; E. KM survival curve for the high- and low-score groups of patients in the IMvigor210 dataset; F-H. Different PD1 response rate based on different algorithms.

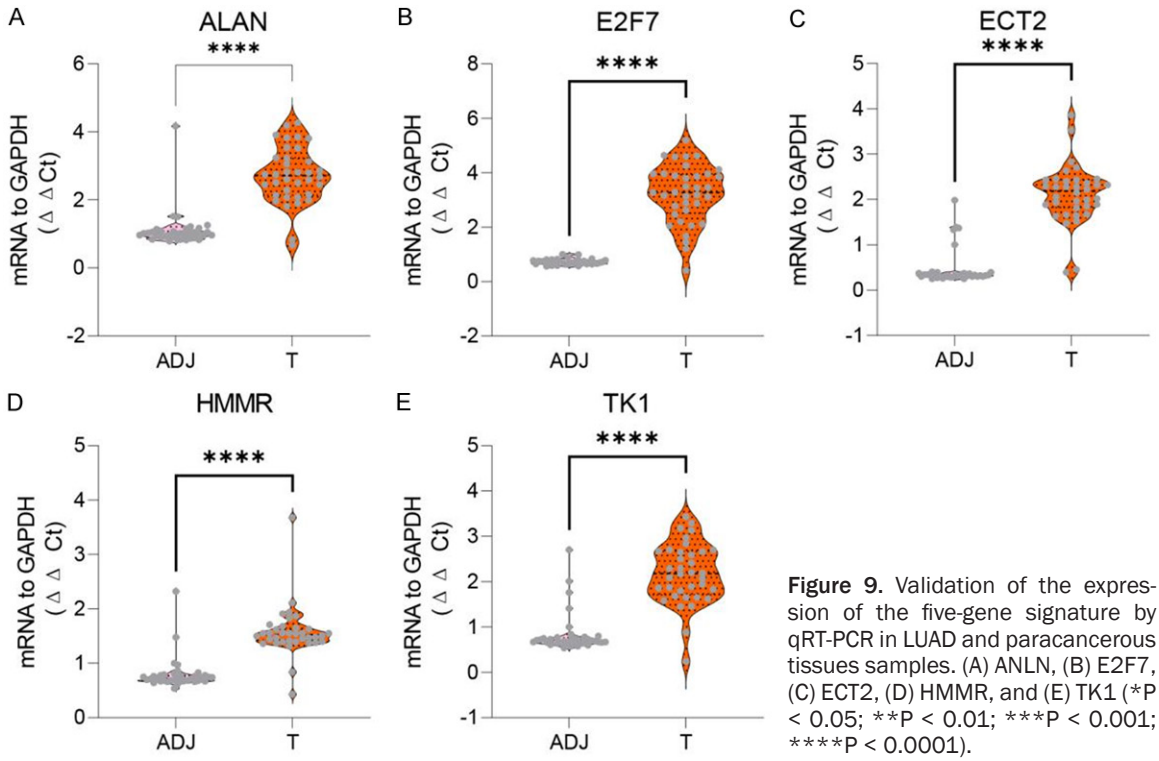

Figure 9. Validation of the expression of the five-gene signature by qRT-PCR in LUAD and paracancerous tissues samples. (A) ANLN, (B) E2F7, (C) ECT2, (D) HMMR, and (E) TK1 (*P < 0.05; **P < 0.01; ***P < 0.001; ****P < 0.0001).

use not only qRT-PCR to determine their transcription level but also histochemical staining to detect the protein expression of these five hub genes in these samples. A paired t-test confirmed that the fluorescence intensity of ANLN, E2F7, ECT2, HMMR, and TK1 in LUAD were significantly higher than that in normal adjacent tissues (**Figure 10A-E**), further demonstrating the reliability and accuracy of the hub genes we screened.

Discussion

Pyroptosis and ferroptosis are emerging as important forms of programmed cell death in normal and pathological conditions including cancer. Ferroptosis and pyroptosis can influence the TIME and suppress the occurrence and the development of cancer, thereby improving the prognosis of patients with cancer [45]. Ferroptosis and pyroptosis can also impact cancer therapy to affect the survival of patients [46]. The commonly used chemotherapeutic drugs and immune checkpoint inhibitors (ICIs) inhibit tumor progression by inducing apoptosis [47]; however, most tumors exhibit innate resistance to apoptosis [48]. Identifying new pathways of cell death induction will lead to the development of potentially new cancer therapy techniques. Therefore, our current studies on the non-apoptotic-related new cell death pathways will shed light on the dvelopment of therapeutic targets.

In this study, we stratified LUAD into four distinct subgroups: immobility, ferroptosis, pyroptosis, and mixed, based on the dual analysis of ferroptosis and pyroptosis-related gene expressions. The pyroptosis subgroup had the greatest patient survival, according to the survival study, while patients in the ferroptosis and mixed subgroups has the worst survival. Significant differences in the immunoreactivities among the subgroups were also observed; the ferroptosis subgroup showed the highest tumor homogeneity and the lowest immune score, while the pyroptosis subgroup showed the opposite features, which might attribute to the different survival among subgroups. Furthermore, there were differences in immunocyte infiltrations among subgroups; the infiltration of CD8+ T cells and memory B cells were higher in the pyroptosis subgroup, while naive B cells and activated dendritic cells were enriched in the ferroptosis subgroup. Thus, our findings provided new insights into the immunological features of different LUAD subgroups.

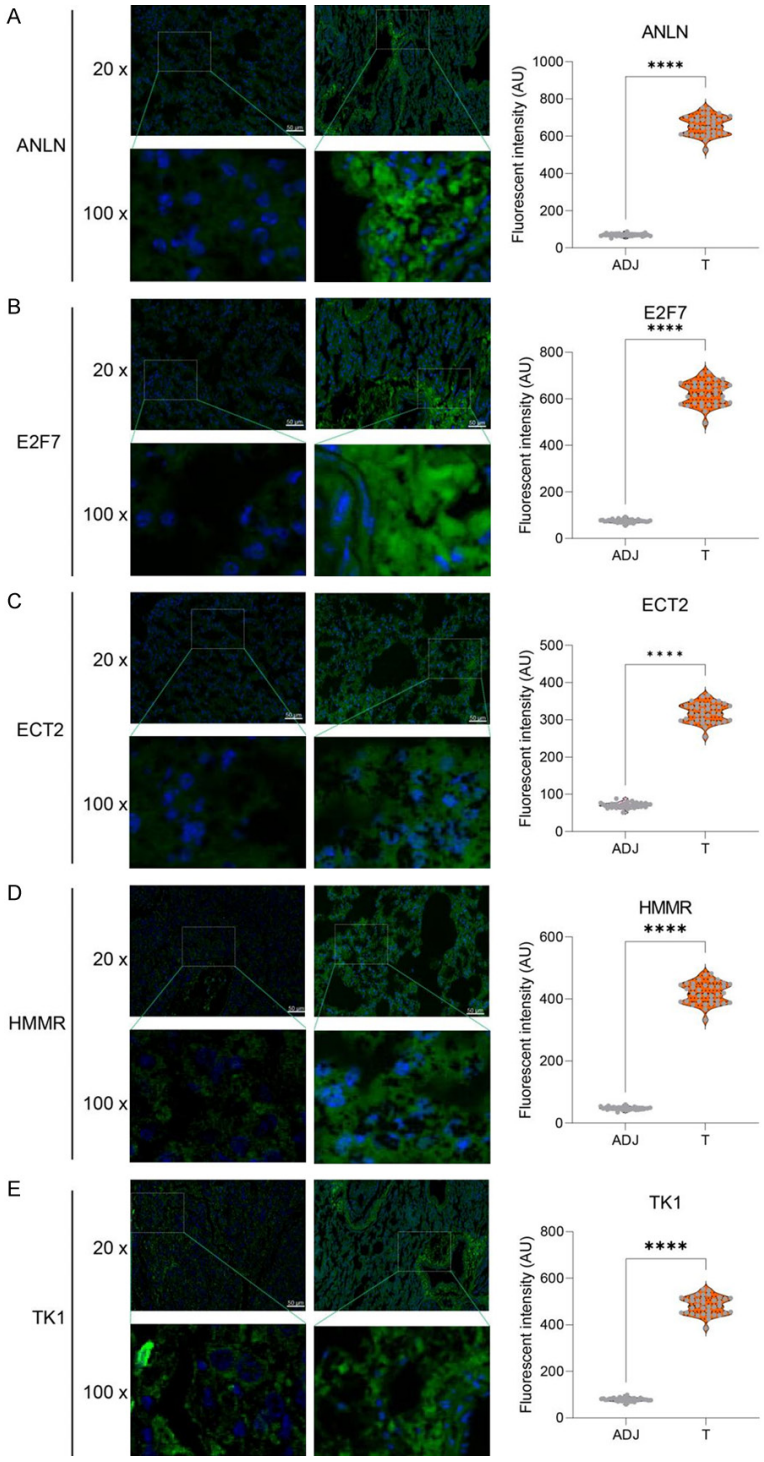

Figure 10. Histochemical staining to detect the expression levels of five hub genes. (A) ANLN, (B) E2F7, (C) ECT2, (D) HMMR, and (E) TK1 (*P < 0.05; **P < 0.01; ***P < 0.001; ****P < 0.0001).

Previous research has shown the significance of genetic alterations in modulating tumor immunity and immune invasion patterns [49]. Thus, we analyzed the differences in copy number variations and somatic variations between different subgroups. Higher TMB was observed in the ferroptosis and mixed subgroups, while TMB in the pyroptosis and immobility subgroups was lower. The chromosome amplification and deletion events were most abundant in the ferroptosis subgroup, while lowest in the pyroptosis subgroup. In addition, a positive correlation between p53 and ferroptosis genes, a negative correlation between TTN and ferroptosis genes, and no significant correlation between TTN and pyroptosis genes were found. The tumour suppressor p53 and ferroptosis sensitivity are tightly related [50]. In p53 wildtype mice, p53 binds to the promoter of SLC7A11, an essential molecule for ferroptosis induction, and inhibits its transcription. But animals carrying numerous p53 mutations (K98R, K117R, K161R, and K162R) show a significant reduction in p53-dependent ferroptosis responses [51]. Ferroptosis is thought to be an innate mechanism for beginning tumour resistance given the high prevalence of p53 mutation in diverse malignancies [52]. Ferroptosis subgroup showed more genomic alterations as compared to the pyroptosis subgroup, and the significantly high association between ferroptosis and mutations may lead to malignant tumor and worse prognosis.

Given the differences in survival and biological functions among the subgroups, we analyzed the differential expression of ferroptosis and pyroptosis genes. Based on the WGCNA co-expression network, we selected the gene

sets that were most relevant to pyroptosis and ferroptosis and finally identified ANLN, E2F7, ECT2, HMMR, and TK1 genes as the signature for the risk model. As a result, based on the median risk score, we divided the samples into high- and low-risk groups, and then we examined the variations between these groups. The development of the risk model should enable the prognostic prediction to be more precise.

Increasing evidence has shown that the immune system may influence cancer in a context-dependent way, either by promoting it or by inhibiting it. Accordingly, one of the most effective anticancer therapies, immune checkpoint therapy, has been developed. In our study, we found significant differences in the immune status of the low- and high-risk LUAD patients. M0/M1 macrophages and activated CD4 cells were found to show high infiltration in the high-risk group, while B cells, dendritic cells, mast cells, plasma cells, resting CD4 cells, and Tregs were enriched in the low-risk group, suggesting the active antigen presentation in the low-risk group. B cells can inhibit tumor cells, reduce the occult micrometastasis incidence, and prolong survival by limiting subsequent tumor spread [53]. Remark et al. have summarized some studies on the relationship between immune cells and survival outcomes in NSCLC and suggested that B cell density was a better prognostic marker [54]. We also observed that immune cell infiltration had a significant effect on LUAD survival outcomes. The degree of B cell infiltration reduced as the risk score went up, which is consistent with the high-risk patients' shorter survival times. To examine the functional mechanisms underlying the gene signature, we performed gene enrichment analysis by utilizing GSEA. Compared to the low-risk group, the high-risk group showed significant enrichment in the activation of the cell cycle, DNA repair, and p53 signaling pathways, suggesting an active cell proliferation in the high-risk group.

We evaluated the effectiveness of employing risk score to forecast the chemotherapeutic response in order to more accurately assess the clinical viability of our risk model. The IC50 values of the five commonly used chemotherapeutic drugs were significantly high in the low-risk score group, suggesting that the patients in this group were less sensitivity to chemotherapy. In addition to chemotherapy, we also determined the relationship between patient characteristics and immunotherapeutic sensitivity. Our results suggested that patients in the low-risk score group were more sensitive to PD1 therapy, consistent with the findings that the characteristics of high-risk score group were significantly related to cell cycle, while those in the low-risk score group were mainly associated with cellular immunity. Collectively, our findings may provide rationales in selecting treatment options for LUAD patients.

In summary, our study has some advantages. First, the combined ferroptosis- and pyroptosis-related gene signatures were identified in the scRNA-seq data of LUAD, which were more accurate than the traditional biomarkers. Second, the risk model could systematically quantify individual LUAD patients from multiple perspectives, including function, immune infiltration, and genomic alterations. Hence, the risk model could perform bettr in predicting the responses to chemotherapy and immunotherapy. Finally, we used external experiments to validate the prognostic value of hub genes in clinical samples.

However, our study has some limitations. The data we used were from the TCGA database and the GEO datasets. All sample information in the four cohorts (TCGA-LUAD and three-GEO cohorts) that were used for construction and external validation of the prognostic signature were also from public databases. The ferroptosis-associated prognostic signature would be more reliable if validated in our center's prospective clinical trial cohort.

Conclusion

In conclusion, we identified four LUAD subgroups based on the expressions of ferroptosis- and pyroptosis-related genes and constructed a risk model comprising of five ferroptosis- and pyroptosis-related genes. The findings of the predictive model indicated greater accuracy for prognostic prediction, which may guide the clinical treatment. Our study may provide insights into the identification of novel therapeutic targets for LAUD and contribute to the development of individualized therapies targeting unique tumor metabolic characteristics.

Acknowledgements

The authors hereby express their gratitude to all participants who supported the study. This work was supported by Natural Science Foundation of Jiangsu Province (Youth Found) (BK20200395) and National Natural Science Foundation of China (Youth Found) (82103309).

The study was approved by Shanghai Pulmonary Hospital Ethics Committee (K21-111Y). The patients consented to participate.

Disclosure of conflict of interest

None.

Abbreviations

LUAD, Lung adenocarcinoma; ROS, reactive oxygen specie; TCGA, The Cancer Genome Atla; FPKM, Fragments Per Kilobase per Million; TPM, Transcripts Per Kilobase per Million; CNV, copy number variants; GDSC, Genomics of Drug Sensitivity in Cancer; RR, ridge regression; IC50, half-maximal inhibitory concentration; TIDE, Tumor Immune Dysfunction and Exclusion; MOA, mode of action; tROC, time-dependent receiver operating characteristic; AUC, area under the curve; TMB, tumor mutation burden; ROS, reactive oxygen species; NO, nitric oxide; TME, tumor microenvironment; GO, Gene Ontology; KEGG, Kyoto Encyclopedia of Genes and Genomes; DEGs, differentially expressed genes; FDR, false discovery rate.

Address correspondence to: Dr. Wentian Zhang, Department of Thoracic Surgery, Shanghai Pulmonary Hospital, Tongji University School of Medicine, Shanghai 200433, China. E-mail: dr_zhangwentian@163.com; Dr. Shiya Zheng, Department of Oncology, Zhongda Hospital, School of Medicine, Southeast University, Nanjing 210009, China. E-mail: zhengshiya1990@163.com; zhengshiya@seu.edu.cn

References

[1] Sung H, Ferlay J, Siegel RL, Laversanne M, Soerjomataram I, Jemal A and Bray F. Global cancer statistics 2020: GLOBOCAN estimates of incidence and mortality worldwide for 36 cancers in 185 countries. CA Cancer J Clin 2021; 71: 209-249.

[2] Bi K, Wei X, Qin X and Li B. BTK has potential to be a prognostic factor for lung adenocarcinoma and an indicator for tumor microenvironment remodeling: a study based on TCGA data mining. Front Oncol 2020; 10: 424.

[3] Spella M and Stathopoulos GT. Immune resistance in lung adenocarcinoma. Cancers (Basel) 2021; 13: 384.

[4] Naimi A, Mohammed RN, Raji A, Chupradit S, Yumashev AV, Suksatan W, Shalaby MN, Thangavelu L, Kamrava S, Shomali N, Sohrabi AD, Adili A, Noroozi-Aghideh A and Razeghian E. Tumor immunotherapies by immune checkpoint inhibitors (ICIs); the pros and cons. Cell Commun Signal 2022; 20: 44.

[5] Wang Y, Wang Y, Ren Y, Zhang Q, Yi P and Cheng C. Metabolic modulation of immune checkpoints and novel therapeutic strategies in cancer. Semin Cancer Biol 2022; [Epub ahead of print].

[6] Zhao Z, He B, Cai Q, Zhang P, Peng X, Zhang Y, Xie H and Wang X. Combination of tumor mutation burden and immune infiltrates for the prognosis of lung adenocarcinoma. Int Immunopharmacol 2021; 98: 107807.

[7] Lin X, Zhou T, Hu S, Yang L, Yang Z, Pang H, Zhou X, Zhong R, Fang X, Yu Z and Hu K. Prognostic significance of pyroptosis-related factors in lung adenocarcinoma. J Thorac Dis 2022; 14: 654-667.

[8] Xiong R, He R, Liu B, Jiang W, Wang B, Li N and Geng Q. Ferroptosis: a new promising target for lung cancer therapy. Oxid Med Cell Longev 2021; 2021: 8457521.

[9] Li S and Huang Y. Ferroptosis: an iron-dependent cell death form linking metabolism, diseases, immune cell and targeted therapy. Clin Transl Oncol 2022; 24: 1-12.

[10] Jiang X, Stockwell BR and Conrad M. Ferroptosis: mechanisms, biology and role in disease. Nat Rev Mol Cell Biol 2021; 22: 266-282.

[11] Alvarez SW, Sviderskiy VO, Terzi EM, Papagiannakopoulos T, Moreira AL, Adams S, Sabatini DM, Birsoy K and Possemato R. NFS1 undergoes positive selection in lung tumours and protects cells from ferroptosis. Nature 2017; 551: 639-643.

[12] Zhang W, Sun Y, Bai L, Zhi L, Yang Y, Zhao Q, Chen C, Qi Y, Gao W, He W, Wang L, Chen D, Fan S, Chen H, Piao H, Qiao Q, Xu Z, Zhang J, Zhao J, Zhang S, Yin Y, Peng C, Li X, Liu Q, Liu H and Wang Y. RBMS1 regulates lung cancer ferroptosis through translational control of SLC7A11. J Clin Invest 2021; 131: e152067.

[13] Wang X, Chen Y, Wang X, Tian H, Wang Y, Jin J, Shan Z, Liu Y, Cai Z, Tong X, Luan Y, Tan X, Luan B, Ge X, Ji H, Jiang X and Wang P. Stem cell factor SOX2 confers ferroptosis resistance in lung cancer via upregulation of SLC7A11. Cancer Res 2021; 81: 5217-5229.

[14] Tang Z, Jiang W, Mao M, Zhao J, Chen J and Cheng N. Deubiquitinase USP35 modulates ferroptosis in lung cancer via targeting ferroportin. Clin Transl Med 2021; 11: e390.
[15] Chen P, Wu Q, Feng J, Yan L, Sun Y, Liu S, Xiang Y, Zhang M, Pan T, Chen X, Duan T, Zhai L, Zhai B, Wang W, Zhang R, Chen B, Han X, Li Y, Chen L, Liu Y, Huang X, Jin T, Zhang W, Luo H, Chen X, Li Y, Li Q, Li G, Zhang Q, Zhuo L, Yang Z, Tang H, Xie T, Ouyang X and Sui X. Erianin, a novel dibenzyl compound in Dendrobium extract, inhibits lung cancer cell growth and migration via calcium/calmodulin-dependent ferroptosis. Signal Transduct Target Ther 2020; 5: 51.
[16] Wang Y, Yu L, Ding J and Chen Y. Iron metabolism in cancer. Int J Mol Sci 2018; 20: 95.
[17] Ye L, Jin F, Kumar SK and Dai Y. The mechanisms and therapeutic targets of ferroptosis in cancer. Expert Opin Ther Targets 2021; 11: 965-986.
[18] Wang W, Green M, Choi JE, Gijón M, Kennedy PD, Johnson JK, Liao P, Lang X, Kryczek I, Sell A, Xia H, Zhou J, Li G, Li J, Li W, Wei S, Vatan L, Zhang H, Szeliga W, Gu W, Liu R, Lawrence TS, Lamb C, Tanno Y, Cieslik M, Stone E, Georgiou G, Chan TA, Chinnaiyan A and Zou W. CD8(+) T cells regulate tumour ferroptosis during cancer immunotherapy. Nature 2019; 569: 270-274.
[19] Lai Y, Zhang Z, Li J, Li W, Huang Z, Zhang C, Li X and Zhao J. STYK1/NOK correlates with ferroptosis in non-small cell lung carcinoma. Biochem Biophys Res Commun 2019; 519: 659-666.
[20] Yang F, Bettadapura SN, Smeltzer MS, Zhu H and Wang S. Pyroptosis and pyroptosis-inducing cancer drugs. Acta Pharmacol Sin 2022; [Epub ahead of print].
[21] Agard NJ, Maltby D and Wells JA. Inflammatory stimuli regulate caspase substrate profiles. Mol Cell Proteomics 2010; 9: 880-893.
[22] Kayagaki N, Stowe IB, Lee BL, O'Rourke K, Anderson K, Warming S, Cuellar T, Haley B, Roose-Girma M, Phung QT, Liu PS, Lill JR, Li H, Wu J, Kummerfeld S, Zhang J, Lee WP, Snipas SJ, Salvesen GS, Morris LX, Fitzgerald L, Zhang Y, Bertram EM, Goodnow CC and Dixit VM. Caspase-11 cleaves gasdermin D for non-canonical inflammasome signalling. Nature 2015; 526: 666-671.
[23] Shi J, Zhao Y, Wang K, Shi X, Wang Y, Huang H, Zhuang Y, Cai T, Wang F and Shao F. Cleavage of GSDMD by inflammatory caspases determines pyroptotic cell death. Nature 2015; 526: 660-665.
[24] Crawford ED and Wells JA. Caspase substrates and cellular remodeling. Annu Rev Biochem 2011; 80: 1055-1087.
[25] Miguchi M, Hinoi T, Shimomura M, Adachi T, Saito Y, Niitsu H, Kochi M, Sada H, Sotomaru Y, Ikenoue T, Shigeyasu K, Tanakaya K, Kitadai Y, Sentani K, Oue N, Yasui W and Ohdan H. Gasdermin c is upregulated by inactivation of transforming growth factor β receptor type II in the presence of mutated apc, promoting colorectal cancer proliferation. PLoS One 2016; 11: e166422.
[26] Gao J, Qiu X, Xi G, Liu H, Zhang F, Lv T and Song Y. Downregulation of GSDMD attenuates tumor proliferation via the intrinsic mitochondrial apoptotic pathway and inhibition of EGFR/Akt signaling and predicts a good prognosis in non-small cell lung cancer. Oncol Rep 2018; 40: 1971-1984.
[27] Teng J, Mei Q, Zhou X, Tang Y, Xiong R, Qiu W, Pan R, Law BY, Wong VK, Yu C, Long H, Xiao X, Zhang F, Wu J, Qin D and Wu A. Polyphyllin VI induces caspase-1-mediated pyroptosis via the induction of ROS/NF-κB/NLRP3/GSDMD signal axis in non-small cell lung cancer. Cancers (Basel) 2020; 12: 193.
[28] Zhang C, Li C, Wang Y, Xu L, He X, Zeng Q, Zeng C, Mai F, Hu B and Ouyang D. Chemotherapeutic paclitaxel and cisplatin differentially induce pyroptosis in A549 lung cancer cells via caspase-3/GSDME activation. Apoptosis 2019; 24: 312-325.
[29] Yuan R, Zhao W, Wang Q, He J, Han S, Gao H, Feng Y and Yang S. Cucurbitacin B inhibits non-small cell lung cancer in vivo and in vitro by triggering TLR4/NLRP3/GSDMD-dependent pyroptosis. Pharmacol Res 2021; 170: 105748.
[30] Lin W, Chen Y, Wu B, Chen Y and Li Z. Identification of the pyroptosis-related prognostic gene signature and the associated regulation axis in lung adenocarcinoma. Cell Death Discov 2021; 7: 161.
[31] Zhang Z, Zhang Y, Xia S, Kong Q, Li S, Liu X, Junqueira C, Meza-Sosa KF, Mok TMY, Ansara J, Sengupta S, Yao Y, Wu H and Lieberman J. Gasdermin E suppresses tumour growth by activating anti-tumour immunity. Nature 2020; 579: 415-420.
[32] Stockwell BR and Jiang X. A physiological function for ferroptosis in tumor suppression by the immune system. Cell Metab 2019; 30: 14-15.
[33] Tang R, Xu J, Zhang B, Liu J, Liang C, Hua J, Meng Q, Yu X and Shi S. Ferroptosis, necroptosis, and pyroptosis in anticancer immunity. J Hematol Oncol 2020; 13: 110.
[34] Karki R and Kanneganti T. Diverging inflammasome signals in tumorigenesis and potential targeting. Nat Rev Cancer 2019; 19: 197-214.
[35] Xia X, Wang X, Cheng Z, Qin W, Lei L, Jiang J and Hu J. The role of pyroptosis in cancer: pro-cancer or pro-"host"? Cell Death Dis 2019; 10: 650.

[36] Man SM and Kanneganti T. Regulation of inflammasome activation. Immunol Rev 2015; 265: 6-21.
[37] Stockwell BR, Friedmann Angeli JP, Bayir H, Bush AI, Conrad M, Dixon SJ, Fulda S, Gascón S, Hatzios SK, Kagan VE, Noel K, Jiang X, Linkermann A, Murphy ME, Overholtzer M, Oyagi A, Pagnussat GC, Park J, Ran Q, Rosenfeld CS, Salnikow K, Tang D, Torti FM, Torti SV, Toyokuni S, Woerpel KA and Zhang DD. Ferroptosis: a regulated cell death nexus linking metabolism, redox biology, and disease. Cell 2017; 171: 273-285.
[38] Hassannia B, Vandenabeele P and Vanden Berghe T. Targeting ferroptosis to iron out cancer. Cancer Cell 2019; 35: 830-849.
[39] Bersuker K, Hendricks JM, Li Z, Magtanong L, Ford B, Tang PH, Roberts MA, Tong B, Maimone TJ, Zoncu R, Bassik MC, Nomura DK, Dixon SJ and Olzmann JA. The CoQ oxidoreductase FSP1 acts parallel to GPX4 to inhibit ferroptosis. Nature 2019; 575: 688-692.
[40] Schröder MS, Culhane AC, Quackenbush J and Haibe-Kains B. Survcomp: an R/Bioconductor package for performance assessment and comparison of survival models. Bioinformatics (Oxford, England) 2011; 27: 3206-3208.
[41] Ayers M, Lunceford J, Nebozhyn M, Murphy E, Loboda A, Kaufman DR, Albright A, Cheng JD, Kang SP, Shankaran V, Piha-Paul SA, Yearley J, Seiwert TY, Ribas A and Mcclanahan TK. IFN-γ-related mRNA profile predicts clinical response to PD-1 blockade. J Clin Invest 2017; 127: 2930-2940.
[42] Hugo W, Zaretsky JM, Sun L, Song C, Moreno BH, Hu-Lieskovan S, Berent-Maoz B, Pang J, Chmielowski B, Cherry G, Seja E, Lomeli S, Kong X, Kelley MC, Sosman JA, Johnson DB, Ribas A and Lo RS. Genomic and transcriptomic features of response to anti-PD-1 therapy in metastatic melanoma. Cell 2016; 165: 35-44.
[43] De Santa F, Vitiello L, Torcinaro A and Ferraro E. The role of metabolic remodeling in macrophage polarization and its effect on skeletal muscle regeneration. Antioxid Redox Signal 2019; 30: 1553-1598.
[44] Lee C, Lee J, Choi SA, Kim S, Wang K, Park S, Kim SH, Lee JY and Phi JH. M1 macrophage recruitment correlates with worse outcome in SHH Medulloblastomas. BMC Cancer 2018; 18: 535.
[45] Yu J, Wang Q, Zhang X, Guo Z and Cui X. Mechanisms of neoantigen-targeted induction of pyroptosis and ferroptosis: from basic research to clinical applications. Front Oncol 2021; 11: 685377.
[46] Yang B, Zhong W, Gu Y and Li Y. Emerging mechanisms and targeted therapy of pyroptosis in central nervous system trauma. Front Cell Dev Biol 2022; 10: 832114.
[47] Liu W, Zhang L, Xiu Z, Guo J, Wang L, Zhou Y, Jiao Y, Sun M and Cai J. Combination of immune checkpoint inhibitors with chemotherapy in lung cancer. Onco Targets Ther 2020; 13: 7229-7241.
[48] Sasidharan Nair V and Elkord E. Immune checkpoint inhibitors in cancer therapy: a focus on T-regulatory cells. Immunol Cell Biol 2018; 1: 21-33.
[49] Cindy Yang SY, Lien SC, Wang BX, Clouthier DL, Hanna Y, Cirlan I, Zhu K, Bruce JP, El Ghamrasni S, Iafolla MAJ, Oliva M, Hansen AR, Spreafico A, Bedard PL, Lheureux S, Razak A, Speers V, Berman HK, Aleshin A, Haibe-Kains B, Brooks DG, Mcgaha TL, Butler MO, Bratman SV, Ohashi PS, Siu LL and Pugh TJ. Pan-cancer analysis of longitudinal metastatic tumors reveals genomic alterations and immune landscape dynamics associated with pembrolizumab sensitivity. Nat Commun 2021; 12: 5137.
[50] Kang R, Kroemer G and Tang D. The tumor suppressor protein p53 and the ferroptosis network. Free Radic Biol Med 2019; 133: 162-168.
[51] Wang S, Li D, Ou Y, Jiang L, Chen Y, Zhao Y and Gu W. Acetylation is crucial for p53-mediated ferroptosis and tumor suppression. Cell Rep 2016; 17: 366-373.
[52] Bykov VJN, Eriksson SE, Bianchi J and Wiman KG. Targeting mutant p53 for efficient cancer therapy. Nat Rev Cancer 2018; 18: 89-102.
[53] Bremnes RM, Al-Shibli K, Donnem T, Sirera R, Al-Saad S, Andersen S, Stenvold H, Camps C and Busund L. The role of tumor-infiltrating immune cells and chronic inflammation at the tumor site on cancer development, progression, and prognosis: emphasis on non-small cell lung cancer. J Thorac Oncol 2011; 6: 824-833.
[54] Remark R, Becker C, Gomez JE, Damotte D, Dieu-Nosjean M, Sautès-Fridman C, Fridman W, Powell CA, Altorki NK, Merad M and Gnjatic S. The non-small cell lung cancer immune contexture. A major determinant of tumor characteristics and patient outcome. Am J Respir Crit Care Med 2015; 191: 377-390.

Table S1. Pyroptotic and Ferroptosis genes obtained from previously published reviews

Ferroptosis genes	Pyroptosis genes
ABCC1	AIM2
ACACA	APIP
ACO1	CASP1
ACSF2	CASP3
ACSL1	CASP4
ACSL3	CASP5
ACSL4	CASP6
ACSL5	CASP8
ACSL6	CASP9
AKR1C1	DHX9
AKR1C2	ELANE
AKR1C3	ELAVL1
ALOX12	GPX4
ALOX15	GSDMA
ALOX15B	GSDMB
ANO6	GSDMC
ATF4	GSDMD
ATG5	GZMA
ATG7	GZMB
ATP5G3	IL18
AURKA	IL1B
BAP1	IL6
BECN1	NAIP
CBS	NLRC4
CD44	NLRP1
CDKN1A	NLRP2
CDKN2A	NLRP3
CFTR	NLRP6
CHAC1	NLRP7
CISD1	NLRP9
CP	NOD1
CRYAB	NOD2
CS	PLCG1
CYBB	PRKACA
DPP4	PYCARD
EGLN1	SCAF11
ELAVL1	TIRAP
EMC2	TNF
EPAS1	ZBP1
FADS2	
FANCD2	
FDFT1	
FH	
FTH1	
FTL	
G3BP1	
G6PD	

GCLC
GCLM
GLS2
GOT1
GPX4
GSS
HELLS
HILPDA
HMGB1
HMGCR
HMOX1
HSBP1
HSPA5
HSPB1
IREB2
ITGA6
KEAP1
LAMP2
LINC00472
LOX
LPCAT3
MAP1LC3A
MAP1LC3B
MAP1LC3C
MAP3K5
MAPK1
MDM2
MIF
MT1G
MUC1
MYC
NCOA4
NFE2L2
NFS1
NQO1
OTUB1
PCBP1
PCBP2
PEBP1
PGD
PHKG2
PRKAA1
PRKAA2
PRNP
PTGS2
RB1
RPL8
SAT1
SAT2

SLC11A2
SLC1A5
SLC39A14
SLC39A8
SLC3A2
SLC40A1
SLC7A11
SOCS1
SQLE
STEAP3
TF
TFRC
TP53
TP63
VDAC2
VDAC3
ZEB1

Table S2. Primer Sequences

Target Gene	Primer (5'-3')
ANLN	ATCTACGACACCAGGAGGAACAG
	TCGGCCACGAAGACATGCTA
E2F7	TAGCTCGCTATCCAAGTTATCCC
	TCATAGATGCGTCTCCTTTCCAC
ECT2	GAAAGGCGGAATGAACAGGAT
	CATCTTTCATCTCCAAGCGGT
HMMR	CATGGTGCAGCTCAGGAACA
	AAGCTGACAGCGGAGTTTTG
TK1	AAGCACAGAGTTGATGAGACGC
	GCAGAACTCCACGATGTCAGG
GAPDH	GGAAGCTTGTCATCAATGGAAATC
	TGATGACCCTTTTGGCTCCC

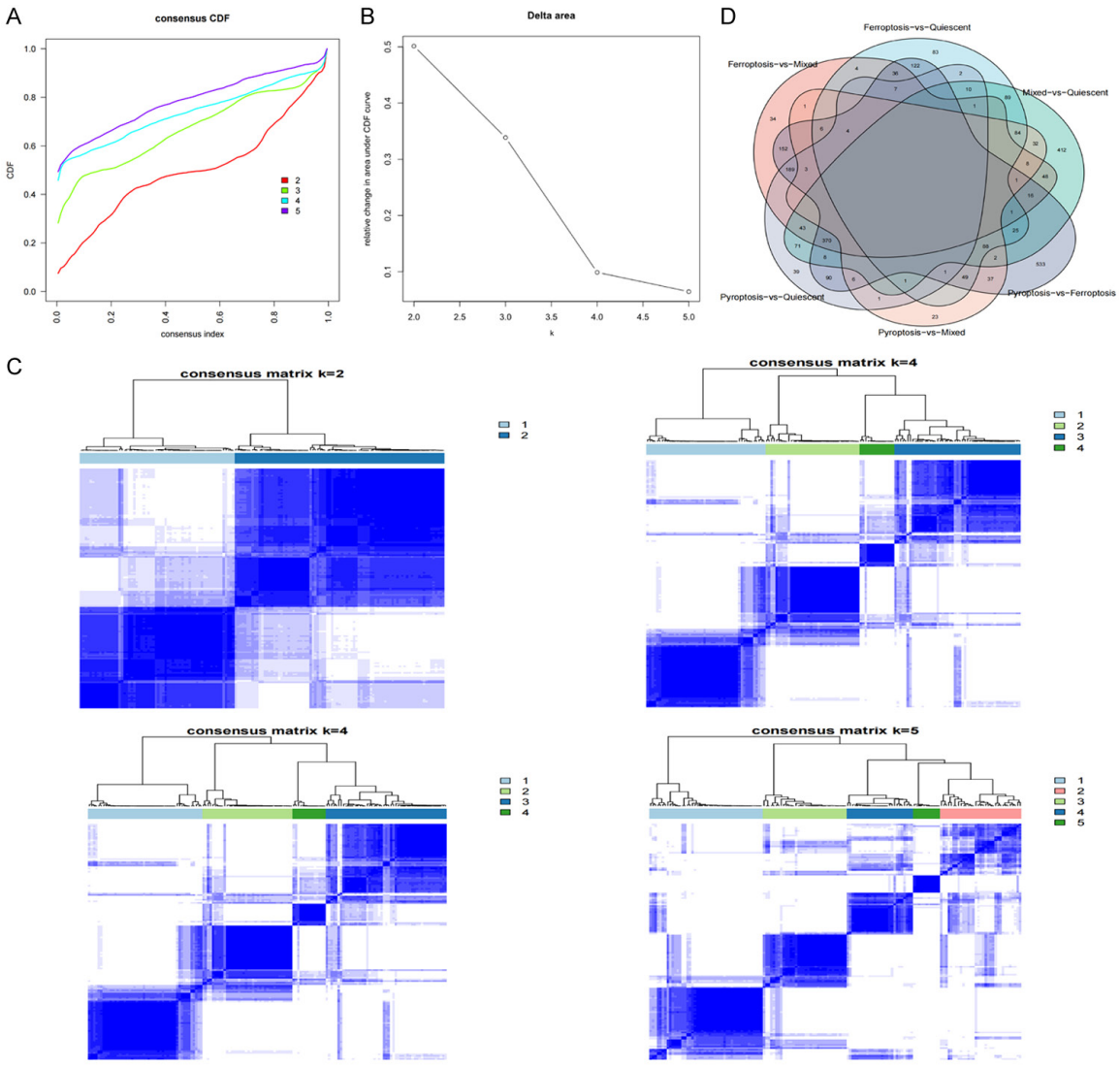

Figure S1. ConsensusClusterPlus clustering. A. K = 2-5 consensus clustering cumulative distribution function; B. The relative change in area under the CDF curve for k = 2-5; C. Correlation between among subgroups; D. Venn diagram of intersecting differentially expressed genes among the four subgroups.

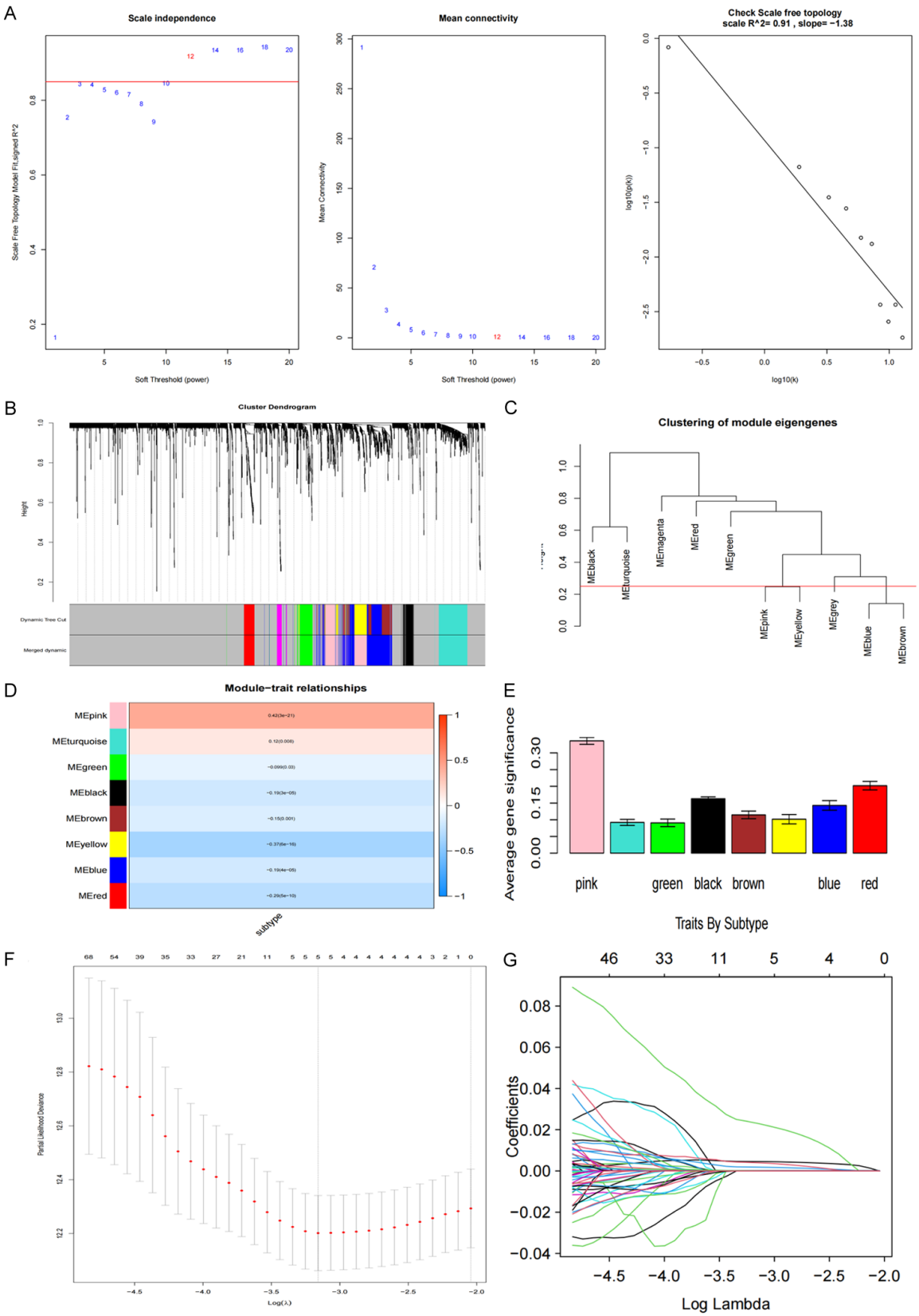

Figure S2. WGCNA module analyses. A. Non-index analysis for various values of soft threshold power (β). Average connectivity analysis for various values of soft threshold power. Scale-free topology (left panel). The x-axis showed the logarithm of the overall network connectivity, while the y-axis showed the logarithm of the corresponding fre-

quency distribution (right panel). On this graph, the distribution was closed to an approximately straight line, namely an approximate scale-free topology; B. Genetic clustering tree graph based on the topological overlap. Different colors were assigned to the corresponding modules; C. Sample cluster analysis; D. Analysis of the correlations between the genes in the heat map modules and iron death score subgroups; E. Correlation among genes in different modules and phenotypes; F, G. Lasso regression.

Table S5. The Candidate prognostic gene

Output of the Cox regression						Output of Kaplan-Meier Survival Analysis	
gene	HR	z	*p* value	lower	upper	gene	*p* value
ANLN	1.010589	5.941821	2.82E-09	1.007084	1.014106	ANLN	4.03E-06
E2F7	1.088375	5.552556	2.82E-08	1.056322	1.1214	KIF23	6.61E-06
HMMR	1.023312	4.843561	1.28E-06	1.013814	1.032899	FAM72C	8.48E-06
ECT2	1.009464	4.708779	2.49E-06	1.005514	1.01343	HMMR	8.82E-06
KIF18A	1.056475	4.640301	3.48E-06	1.032242	1.081277	CDK1	1.48E-05
CCNB1	1.005463	4.529929	5.90E-06	1.003096	1.007836	TK1	1.52E-05
CDC25C	1.054555	4.409641	1.04E-05	1.029949	1.07975	PLK1	1.90E-05
PLK1	1.015046	4.368727	1.25E-05	1.008268	1.02187	CASC5	2.07E-05
EXO1	1.023587	4.354819	1.33E-05	1.012903	1.034383	DEPDC1B	2.81E-05
KPNA2	1.00296	4.317056	1.58E-05	1.001615	1.004307	CDC25C	3.04E-05
DLGAP5	1.012719	4.279065	1.88E-05	1.006873	1.018598	GTSE1	3.10E-05
RRM2	1.007227	4.27102	1.95E-05	1.003904	1.01056	HJURP	3.25E-05
PRC1	1.013625	4.227	2.37E-05	1.007284	1.020005	SKA3	3.38E-05
FEN1	1.008582	4.15507	3.25E-05	1.004525	1.012656	PRC1	5.52E-05
KIF20A	1.01524	4.151928	3.30E-05	1.008017	1.022514	ARHGAP11A	6.10E-05
KIF4A	1.018571	4.148119	3.35E-05	1.009754	1.027465	TYMS	7.35E-05
DTL	1.029359	4.14722	3.37E-05	1.015378	1.043532	FAM72B	7.51E-05
TK1	1.00291	4.06628	4.78E-05	1.001506	1.004315	OIP5	9.49E-05
CDKN3	1.01549	4.064763	4.81E-05	1.007991	1.023044	FAM83D	9.91E-05
NEK2	1.014812	4.048592	5.15E-05	1.007614	1.022061	ECT2	0.000124
CCNA2	1.009024	4.047682	5.17E-05	1.004644	1.013422	SGOL2	0.000125
SHCBP1	1.031316	4.016965	5.90E-05	1.015916	1.04695	RRM2	0.000125
SKA3	1.032215	3.994251	6.49E-05	1.01628	1.0484	KIF14	0.000128
CDCA5	1.012225	3.933591	8.37E-05	1.006115	1.018371	SHCBP1	0.000138
DIAPH3	1.057546	3.929298	8.52E-05	1.028439	1.087477	CDCA3	0.000139
C18orf54	1.118526	3.914006	9.08E-05	1.057514	1.183057	BUB1B	0.000145
TYMS	1.006851	3.848523	0.000119	1.003356	1.010358	INCENP	0.000147
TUBA1B	1.001834	3.813621	0.000137	1.000891	1.002778	KIF18A	0.000152
ARHGAP11A	1.023102	3.807889	0.00014	1.011145	1.035201	TTK	0.000164
TUBA1C	1.00488	3.799	0.000145	1.002359	1.007407	DIAPH3	0.000165
SPC25	1.025819	3.790748	0.00015	1.012387	1.039429	BRCA2	0.000165
AURKA	1.008555	3.77903	0.000157	1.004109	1.013021	CCNA2	0.000172
HJURP	1.015735	3.769508	0.000164	1.007523	1.024015	KIF20A	0.000173
CKAP2L	1.031866	3.751287	0.000176	1.015092	1.048917	TUBA1B	0.000175
OIP5	1.026878	3.73355	0.000189	1.012679	1.041275	NCAPG	0.000183
SGOL2	1.040931	3.713451	0.000204	1.019123	1.063206	NUSAP1	0.000184
FOXM1	1.007799	3.657378	0.000255	1.003612	1.012003	CENPK	0.000186
CDCA2	1.04156	3.63936	0.000273	1.018968	1.064653	ESPL1	0.000225
PRR11	1.017409	3.628902	0.000285	1.007969	1.026937	BIRC5	0.000247
FANCI	1.020878	3.623015	0.000291	1.00953	1.032353	E2F7	0.00026
NDC80	1.014269	3.565875	0.000363	1.006401	1.022199	NEK2	0.000268

CCNB2	1.010722	3.560597	0.00037	1.004806	1.016673	FAM64A	0.000281
FAM72A	1.294295	3.558445	0.000373	1.122862	1.491903	CDKN3	0.000301
TPX2	1.003096	3.5365	0.000405	1.001379	1.004816	CDCA2	0.000304
TACC3	1.00779	3.475276	0.00051	1.003389	1.012211	CENPU	0.000307
RAD51	1.030215	3.466128	0.000528	1.013019	1.047702	KIF11	0.000309
CENPN	1.032942	3.456959	0.000546	1.014134	1.052098	KIAA0101	0.000317
MKI67	1.010329	3.456163	0.000548	1.004458	1.016233	KPNA2	0.00032
LMNB1	1.00541	3.437168	0.000588	1.002321	1.008507	MAD2L1	0.000329
TICRR	1.077645	3.412449	0.000644	1.032341	1.124937	C16orf59	0.000342
PBK	1.011113	3.403557	0.000665	1.004698	1.017568	TACC3	0.000392
CENPU	1.013642	3.369861	0.000752	1.005685	1.021662	C18orf54	0.000425
BIRC5	1.006587	3.358997	0.000782	1.002738	1.01045	NUF2	0.000429
GTSE1	1.026846	3.352448	0.000801	1.011065	1.042874	FOXM1	0.000436
BORA	1.043543	3.349176	0.000811	1.017837	1.0699	SGOL1	0.000439
MCM4	1.005244	3.331704	0.000863	1.002156	1.008342	RACGAP1	0.00047
CHEK1	1.022661	3.326583	0.000879	1.009248	1.036252	MCM4	0.000484
ORC1	1.024345	3.31991	0.0009	1.009902	1.038995	DEPDC1	0.000521
MAD2L1	1.018967	3.319842	0.000901	1.007726	1.030333	WDHD1	0.000616
CDC25A	1.036722	3.300356	0.000966	1.014754	1.059165	ZWINT	0.000647
CDC20	1.003352	3.293046	0.000991	1.001356	1.005353	ZNF367	0.000665
ESCO2	1.10371	3.247043	0.001166	1.039889	1.171448	CCNB1	0.000688
KIF23	1.017442	3.241431	0.001189	1.006859	1.028135	PKMYT1	0.000726
MCM6	1.006223	3.222083	0.001273	1.002433	1.010028	FAM72D	0.00073
DEPDC1	1.025574	3.192253	0.001412	1.009796	1.041599	HELLS	0.000748
GSG2	1.06808	3.188099	0.001432	1.025697	1.112215	TPX2	0.000763
SKA1	1.022936	3.187476	0.001435	1.008771	1.0373	DLGAP5	0.000771
MELK	1.011099	3.185738	0.001444	1.004256	1.017988	EXO1	0.000798
SMC2	1.017104	3.172098	0.001513	1.006502	1.027818	FAM111B	0.000813
ASF1B	1.007603	3.168138	0.001534	1.002893	1.012336	SPAG5	0.000826
CEP55	1.008615	3.163841	0.001557	1.003269	1.013989	SPC25	0.000861
KIF14	1.033755	3.157749	0.00159	1.012672	1.055276	KIF20B	0.000874
FAM111B	1.015955	3.143621	0.001669	1.005978	1.026031	CCNB2	0.000971
NCAPG	1.015253	3.135946	0.001713	1.005693	1.024904	KIF4A	0.001071
WDHD1	1.017021	3.125531	0.001775	1.006314	1.027843	PLK4	0.001083
KIF11	1.010994	3.116198	0.001832	1.004065	1.017971	KIFC1	0.001175
CDCA3	1.034128	3.113397	0.001849	1.01251	1.056208	MTFR2	0.001203
PRKDC	1.004928	3.10786	0.001884	1.001817	1.008049	TRIP13	0.001227
GINS3	1.049413	3.08508	0.002035	1.017745	1.082066	BUB1	0.001419
BUB1	1.012233	3.083606	0.002045	1.00444	1.020086	CKAP2L	0.001423
UBE2T	1.004163	3.066497	0.002166	1.0015	1.006833	NDC80	0.001443
CDK1	1.00678	3.057278	0.002234	1.002428	1.011151	FAM72A	0.001452
CENPF	1.011112	3.044531	0.00233	1.003944	1.018331	CENPE	0.001471
SGOL1	1.046712	3.038113	0.002381	1.016333	1.077998	KIF18B	0.001524
KIAA0101	1.011372	3.037331	0.002387	1.004019	1.018779	TIMELESS	0.001547
ERCC6L	1.055653	3.030993	0.002438	1.019322	1.093278	NCAPG2	0.001557
CKAP2	1.010989	3.029698	0.002448	1.003866	1.018162	MELK	0.001596
NCAPD2	1.004717	3.010859	0.002605	1.001644	1.0078	CHEK1	0.001606
RFC3	1.01401	3.000963	0.002691	1.004838	1.023267	UBE2T	0.001819
KIF2C	1.00717	2.974653	0.002933	1.00244	1.011923	ATAD2	0.001851
WASF1	1.019858	2.965989	0.003017	1.006692	1.033196	TROAP	0.001856

BUB1B	1.014226	2.953592	0.003141	1.004763	1.023778	PRR11	0.001972
FBXO5	1.028923	2.946346	0.003216	1.009591	1.048625	RAD51	0.00198
CASC5	1.046921	2.945505	0.003224	1.015461	1.079357	SLC38A1	0.002036
INCENP	1.012651	2.931383	0.003375	1.004175	1.021198	CDCA5	0.002157
FAM72B	1.139382	2.919467	0.003506	1.043818	1.243696	WDR76	0.002198
MTHFD2	1.004433	2.912866	0.003581	1.001448	1.007427	ESCO2	0.002271
UHRF1	1.01801	2.912725	0.003583	1.005856	1.03031	PBK	0.002288
NUSAP1	1.005714	2.90824	0.003635	1.00186	1.009583	SMC2	0.002326
CENPE	1.035127	2.861677	0.004214	1.010938	1.059895	TUBA1C	0.002384
RACGAP1	1.008032	2.855298	0.0043	1.002512	1.013582	MTHFD2	0.002569
PKMYT1	1.028239	2.846255	0.004424	1.008709	1.048146	SKA1	0.002604
NCAPH	1.010694	2.829569	0.004661	1.003274	1.018168	FANCD2	0.002676
BLM	1.030046	2.824159	0.00474	1.0091	1.051428	ASF1B	0.002954
FAM64A	1.016595	2.784093	0.005368	1.004884	1.028442	STIL	0.003147
TTK	1.020031	2.777506	0.005478	1.005855	1.034407	CENPW	0.003507
FANCD2	1.042107	2.740729	0.00613	1.011819	1.073301	DSCC1	0.003849
CLSPN	1.02405	2.719283	0.006542	1.006658	1.041743	NCAPH	0.004055
UBE2C	1.001576	2.709519	0.006738	1.000436	1.002718	TOP2A	0.004117
RFC4	1.008795	2.698599	0.006963	1.0024	1.015231	CEP55	0.004256
CDCA8	1.005911	2.697692	0.006982	1.001613	1.010227	CDC45	0.004393
DEPDC1B	1.020554	2.670617	0.007571	1.005429	1.035906	AURKB	0.004435
ZWINT	1.004144	2.665099	0.007697	1.001095	1.007203	CENPF	0.004514
KIF20B	1.029546	2.611015	0.009027	1.007287	1.052296	RAD51AP1	0.005137
WDR76	1.021941	2.600636	0.009305	1.005361	1.038795	GINS1	0.005299
FAM83D	1.008821	2.581219	0.009845	1.002116	1.01557	KIAA1524	0.005441
MTFR2	1.032457	2.571701	0.01012	1.007627	1.057899	FEN1	0.005458
AUNIP	1.026813	2.565499	0.010303	1.006265	1.047781	CDCA8	0.005564
PLK4	1.027795	2.556891	0.010561	1.006421	1.049623	CENPN	0.005587
CDC6	1.008282	2.503041	0.012313	1.001791	1.014815	XRCC2	0.005698
ESPL1	1.023691	2.491093	0.012735	1.005005	1.042725	DTL	0.005753
MCM2	1.004006	2.468216	0.013579	1.000824	1.007198	ASPM	0.005819
SPAG5	1.006911	2.454836	0.014095	1.001389	1.012463	DDIAS	0.006034
ASPM	1.015815	2.419186	0.015555	1.002983	1.02881	MCM10	0.006181
KIAA1524	1.0194	2.378523	0.017382	1.003387	1.035669	UBE2C	0.006416
DSCC1	1.016308	2.365963	0.017983	1.00278	1.030019	AUNIP	0.006499
MCM10	1.020644	2.323777	0.020137	1.003204	1.038387	CDT1	0.006528
CDC45	1.009433	2.306098	0.021105	1.00141	1.017521	PARPBP	0.006611
CENPA	1.011624	2.293724	0.021806	1.001683	1.021664	CDC6	0.006709
PRIM1	1.013737	2.276299	0.022828	1.001898	1.025715	CENPA	0.006728
ZNF367	1.02694	2.273906	0.022972	1.003677	1.050742	IQGAP3	0.006754
RAD51AP1	1.011145	2.249028	0.024511	1.001426	1.020959	GSG2	0.007456
KIFC1	1.004394	2.189114	0.028589	1.000459	1.008345	BRCA1	0.007562
E2F8	1.021008	2.1843	0.02894	1.002138	1.040235	MKI67	0.007893
TRIP13	1.006661	2.159148	0.030839	1.000613	1.012745	TICRR	0.007989
CENPW	1.004358	2.155787	0.0311	1.000395	1.008336	MCM2	0.009194
DDIAS	1.033726	2.152108	0.031389	1.002966	1.065429	TCF19	0.009259
EME1	1.039334	2.152033	0.031395	1.003449	1.076501	ERCC6L	0.00928
CDT1	1.006997	2.147232	0.031775	1.000608	1.013426	FANCI	0.009805
C16orf59	1.024277	2.14643	0.031839	1.002086	1.046959	POLQ	0.010037
SLC38A1	1.004644	2.142188	0.032178	1.000394	1.008913	KIF2C	0.010564

NCAPG2	1.011191	2.132024	0.033005	1.000899	1.021589	ORC1	0.010873
ATAD2	1.006748	2.116493	0.034303	1.000498	1.013038	BORA	0.01092
BRIP1	1.042354	2.066547	0.038777	1.002142	1.08418	CCNE2	0.010942
RAD54L	1.02051	2.062514	0.039159	1.00101	1.04039	CDC20	0.010966
TMEM194A	1.010504	2.05274	0.040098	1.000472	1.020637	MCM6	0.012304
GINS2	1.009489	2.045547	0.040801	1.000395	1.018665	CDC25A	0.013014
TIMELESS	1.0062	2.03773	0.041577	1.000236	1.012199	CDC7	0.013439
AURKB	1.006012	2.021493	0.043229	1.000182	1.011876	BLM	0.013807
CENPK	1.022765	2.018809	0.043507	1.000656	1.045363	NCAPD2	0.017418
RDM1	1.078207	2.004254	0.045043	1.001665	1.160597	UHRF1	0.017878
FAM72D	1.134779	1.979479	0.047762	1.001247	1.286118	GAS2L3	0.01889
CENPI	1.028556	1.970711	0.048757	1.000154	1.057766	FANCA	0.020634
FAM72C	1.186615	1.957726	0.050262	0.999804	1.40833	E2F8	0.022276
TROAP	1.009835	1.932638	0.053281	0.999862	1.019909	RFC3	0.024489
PARPBP	1.025594	1.894086	0.058214	0.999121	1.052768	MYBL2	0.025176
GINS1	1.009655	1.869924	0.061494	0.999537	1.019874	CKAP2	0.025802
KIF15	1.019679	1.852323	0.06398	0.998868	1.040923	KIF15	0.029731
FANCA	1.029852	1.849068	0.064448	0.998237	1.062467	MTBP	0.030076
GAS2L3	1.036376	1.83854	0.065983	0.997643	1.076613	EME1	0.032752
NUF2	1.009049	1.749036	0.080285	0.998914	1.019286	RFC4	0.034774
ORC6	1.020773	1.728209	0.083951	0.997247	1.044855	E2F2	0.037558
TOPBP1	1.006693	1.702629	0.088638	0.998992	1.014453	LMNB1	0.040061
CDC7	1.012541	1.682339	0.092503	0.997946	1.027349	CLSPN	0.04458
BRCA1	1.019088	1.677809	0.093384	0.996825	1.041848	E2F1	0.048894
STIL	1.018957	1.656614	0.097597	0.996567	1.041849	GINS2	0.049728
SMC4	1.006033	1.619184	0.105408	0.998735	1.013384	AURKA	0.051726
MYBL2	1.001336	1.615817	0.106134	0.999716	1.002959	CENPI	0.053743
MTBP	1.052068	1.607895	0.107858	0.988947	1.119218	FBXO5	0.054538
ARHGAP11B	1.066441	1.601398	0.109289	0.9857	1.153797	GINS3	0.055573
KIF18B	1.009933	1.538971	0.123811	0.9973	1.022726	KNTC1	0.060723
E2F2	1.02009	1.498957	0.133885	0.993901	1.046968	TOPBP1	0.06451
TOP2A	1.001448	1.483949	0.137823	0.999536	1.003363	DNA2	0.078664
MMS22L	1.05776	1.384255	0.16628	0.976917	1.145293	BRIP1	0.078746
KNTC1	1.013147	1.343325	0.179167	0.994022	1.032639	ORC6	0.079693
BRCA2	1.033074	1.315004	0.188509	0.984168	1.084411	FANCB	0.084103
FANCB	1.057708	1.30364	0.192357	0.972149	1.150798	PRIM1	0.08702
IQGAP3	1.005818	1.301586	0.193058	0.99707	1.014643	WASF1	0.098657
CCNE2	1.018268	1.254239	0.209755	0.989865	1.047487	MMS22L	0.103115
XRCC2	1.016635	1.190068	0.23402	0.989383	1.044638	RAD54L	0.105968
POLQ	1.026618	1.157224	0.247181	0.981942	1.073327	RDM1	0.150613
NCAPD3	1.008604	1.137703	0.255245	0.993828	1.023599	ARHGAP11B	0.166096
TCF19	1.003132	1.033853	0.301205	0.997202	1.009098	PIF1	0.179131
PIF1	1.02466	1.020454	0.307513	0.977821	1.073741	PRKDC	0.236963
DNA2	1.011327	0.996804	0.31886	0.989176	1.033974	SMC4	0.328308
HELLS	1.011628	0.96821	0.332939	0.988228	1.035581	TMEM194A	0.405705
E2F1	1.00133	0.573804	0.5661	0.996795	1.005885	NCAPD3	0.40718
EZH2	1.002891	0.531247	0.595248	0.992266	1.01363	ZNF695	0.412408
ZNF695	1.012202	0.432475	0.665396	0.958069	1.069393	EZH2	0.529731

Table S6. Two gene-signature models

5-genes-model	4-genes-model
ANLN	ANLN
E2F7	E2F7
ECT2	ECT2
HMMR	HMMR
TK1	

Table S7. The Coefficient of the Risk Factor

Gene	Coefficient
ANLN	0.004561126
E2F7	0.023154612
ECT2	0.001854024
HMMR	0.003971949
TK1	9.03E-05

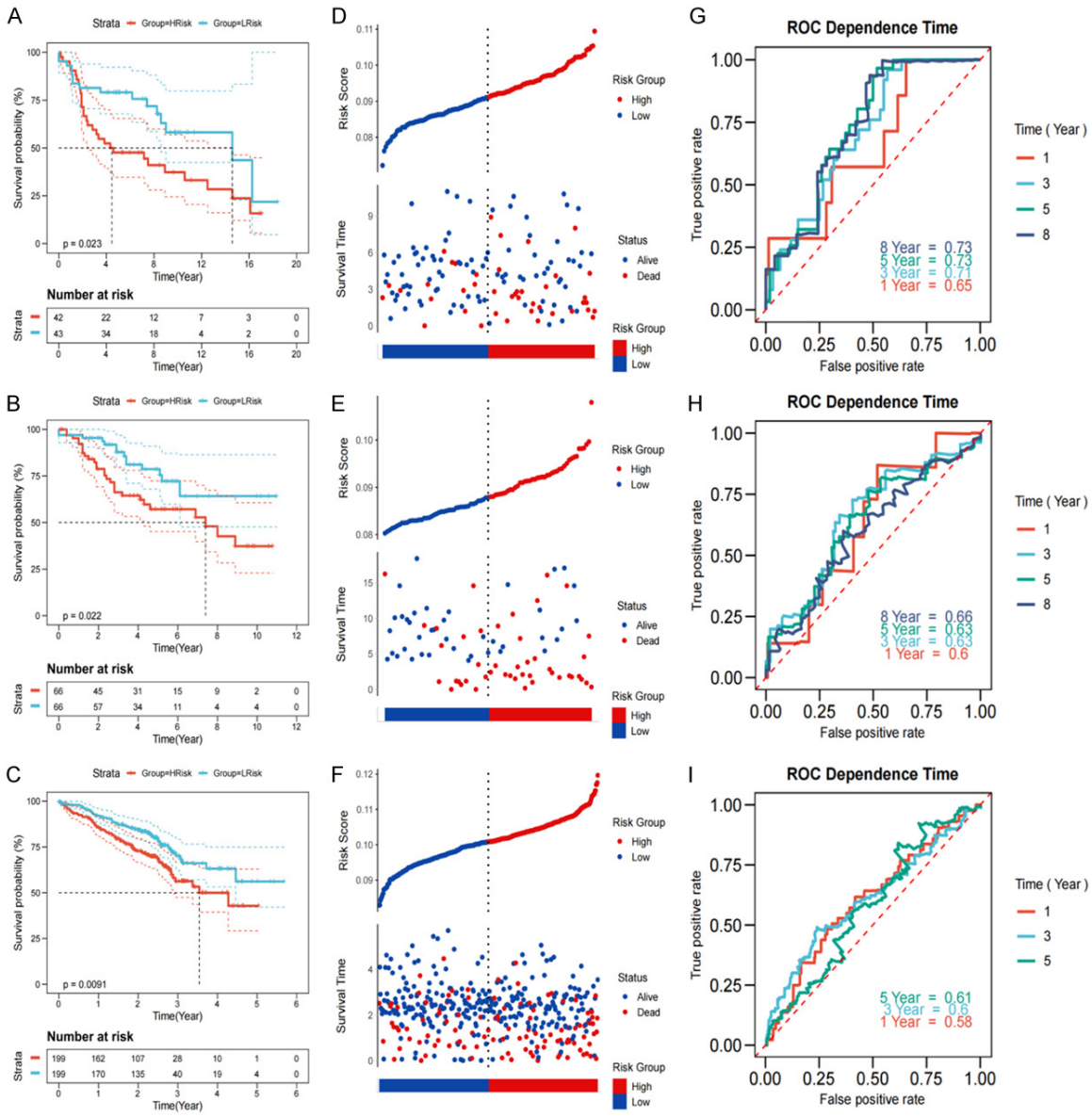

Figure S3. Survival analysis for other data sets. A-C. KM survival curve of the risk scores for patients in GSE30219, GSE42127, and GSE72049 datasets; D-F. Scatter plots of sample survival and risk scores based on GSE30219, GSE42127, and GSE72049 data; G-I. AUC curves for 1, 3, 5, and 8 years based on the risk models for GSE30219, GSE42127, and GSE72049 data sets.

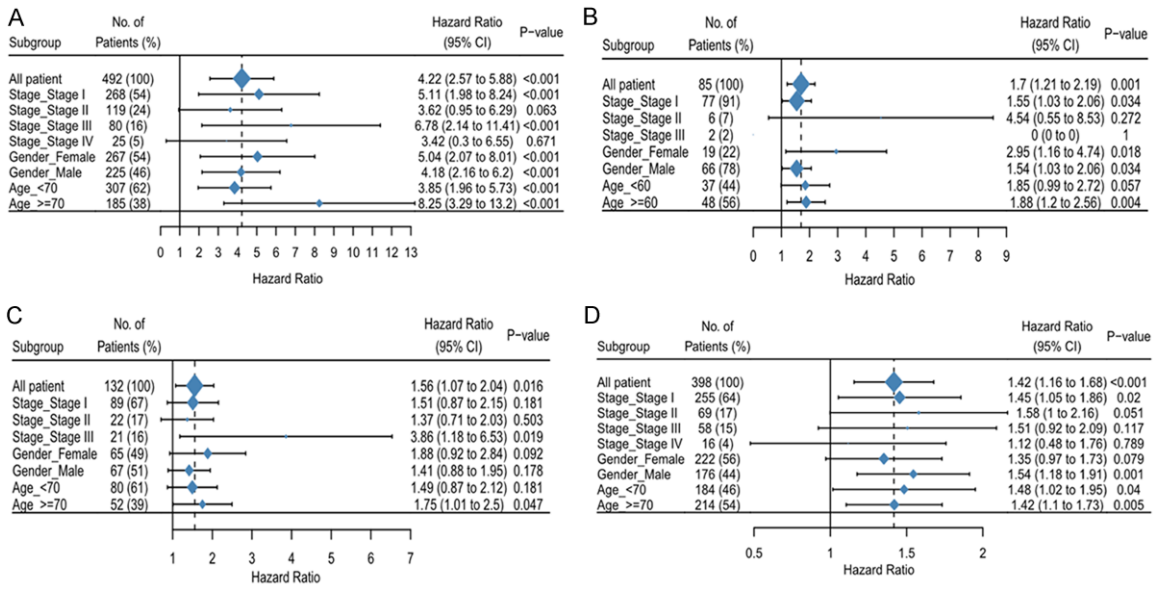

Figure S4. Forest map based on clinical features. (A) TCGA-LUAD, (B) GSE30219, (C) GSE42127, and (D) GSE72094.

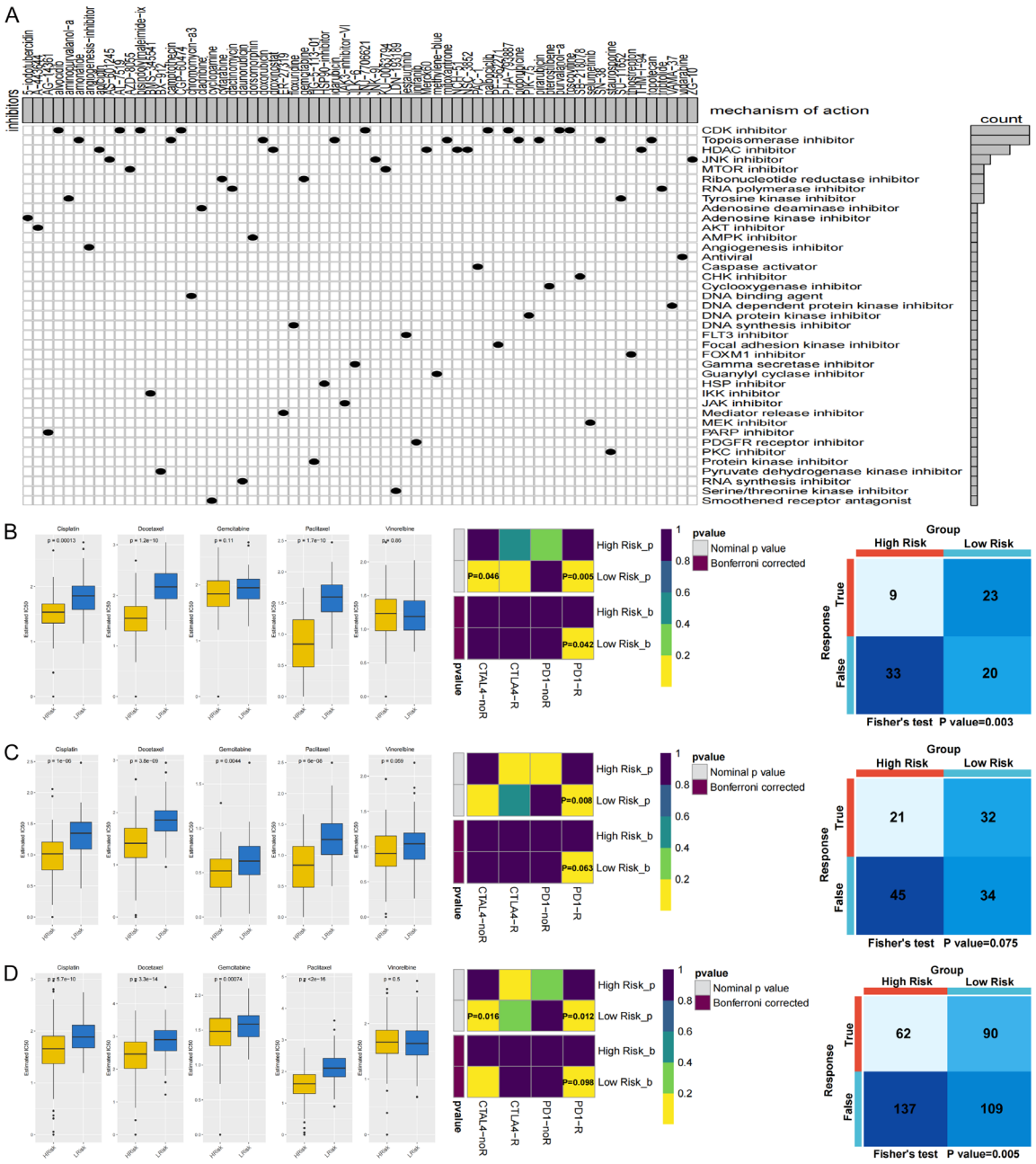

Figure S5. Risk score as an indicator to guide treatment strategies. A. Identification of 66 small molecule drugs targeting 39 molecular pathways by MOA; B-D. Difference in IC50 values between high- and low-score groups and the response rate for PD1 in different score groups; the order from top to bottom is GSE30219, GSE42127, and GSE72094.